




Hyperbolic non-Abelian semimetal

Tarun Tummuru ^{1,*} Anffany Chen ^{2,3} Patrick M. Lenggenhager ^{1,4,5}
Titus Neupert ¹ Joseph Maciejko ^{2,3} and Tomáš Bzdušek ^{1,4,†}

¹Department of Physics, University of Zurich, Winterthurerstrasse 190, 8057 Zurich, Switzerland

²Theoretical Physics Institute, University of Alberta, Edmonton, Alberta T6G 2E1, Canada

³Department of Physics, University of Alberta, Edmonton, Alberta T6G 2E1, Canada

⁴Condensed Matter Theory Group, Paul Scherrer Institute, 5232 Villigen PSI, Switzerland

⁵Institute for Theoretical Physics, ETH Zurich, 8093 Zurich, Switzerland

(Dated: July 20, 2023)

We extend the notion of topologically protected semi-metallic band crossings to hyperbolic lattices in negatively curved space. Due to their distinct translation group structure, such lattices support non-Abelian Bloch states which, unlike conventional Bloch states, acquire a matrix-valued Bloch factor under lattice translations. Combining diverse numerical and analytical approaches, we uncover a quartic scaling in the density of states at low energies, and illuminate a nodal manifold of codimension five in the reciprocal space. The nodal manifold is topologically protected by a non-zero second Chern number, reminiscent of the characterization of Weyl nodes by the first Chern number.

Introduction.—A topological semimetal is defined as a gapless electronic phase with stable band-touching points at the Fermi energy. As solid-state analogs of relativistic fermions, low-energy excitations in a semimetal are often imbued with nontrivial topological properties. Dirac and Weyl semimetals in three dimensions (3D), for instance, exhibit a range of intriguing properties such as protected surface states, anomalous Hall effect, chiral anomaly, and unusual magneto-resistance [1–8]. Broadly, semimetals can be categorized based on spatial dimension, origin of band crossings, and properties of the nodal manifold (e.g., its degeneracy and codimension) [9]. All existing models and material realizations, however, are typically embedded in geometrically flat Euclidean space.

As regular tessellations of 2D hyperbolic space with constant negative curvature, hyperbolic lattices [10] provide the means to systematically study quantum matter in non-Euclidean geometries. Recent realizations of these lattices in coplanar waveguide resonators [11] and topolectrical circuits [12–15] furnish the impetus to understand their physical properties. On the theoretical front, studies of hyperbolic analogs of topological insulators [14–20] show that bulk topological invariants and protected edge modes persist in hyperbolic space. Other celebrated condensed-matter phenomena such as Hofstadter spectra [21, 22], flat bands [23–26], higher-order topology [27–29], strong correlations [30–33], and fractons [34, 35] have also been explored in the hyperbolic context.

Hyperbolic lattices have unique features that open the door to new physics beyond the Euclidean paradigm. Hyperbolic translation groups, known as Fuchsian groups, are non-Abelian [36]. As a result, their unitary irreducible representations (IRs) can have a dimension d larger than one. Via a generalized Bloch theorem, hyperbolic band theory (HBT) [37, 38] provides a reciprocal-space description of hyperbolic lattices and their eigenstates. Hyperbolic Bloch states can be classified as Abelian [U(1)] [37] or non-Abelian [U(d) for $d > 1$] [38, 39]

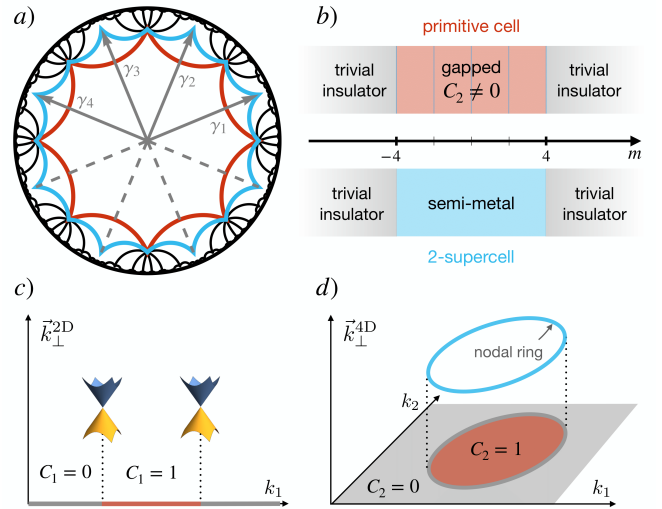


FIG. 1. Real- and reciprocal-space structure of the hyperbolic non-Abelian semimetal. (a) The model is defined on the $\{8, 8\}$ lattice wherein the single- and two-site unit cells are marked in red and blue, respectively. Translation generators of the primitive cell are denoted by γ_j . (b) Unit cell size affects the accessible reciprocal space and, hence, the phase diagram. The primitive cell shows gapped topological phases with $|C_2| = 1$ or 3 , which are separated by transitions at $|m| = 0, 2$. The 2-supercell, in contrast, is gapless in the same parameter range. Both configurations are gapped in the atomic limit, $|m| > 4$. (c) In a Weyl semimetal, 2D planes (along \vec{k}_\perp^{2D}) separating the nodes have a finite first Chern number. (d) In the hyperbolic semimetal, when $|m| \in (3, 4)$, the nodal manifold is a ring that encloses 4D orthogonal subspaces (along \vec{k}_\perp^{4D}) with a nontrivial second Chern number.

depending on the rank d of the matrix-valued Bloch factor acquired under lattice translations. IRs of a given dimension contribute a generalized Brillouin zone (BZ) to the reciprocal space, which can be accordingly referenced as U(1)-BZ or U(d)-BZ. Whereas U(1) eigenstates are labeled by a vector analogous to crystal momentum, additional quantum numbers are required to distinguish U(d) Bloch states. The problem of

* tarun.tummuru@uzh.ch

† tomas.bzusek@uzh.ch

accessing and characterizing non-Abelian Bloch states constitutes an actively investigated topic [40–43].

In this work, we present a hyperbolic lattice model whose semimetallic topology is inherently rooted in non-Abelian Bloch states. While the Abelian spectrum is gapped, we demonstrate the presence of a topologically protected nodal manifold in the non-Abelian Bloch bands, which results in a gapless density of states (DOS) with unconventional scaling. Summarized in Fig. 1, this nodal manifold in reciprocal space is associated with a finite second Chern number C_2 . There is no Euclidean analog of such a phase because 2D Euclidean lattices admit neither non-Abelian Bloch states nor a second Chern number. We term this phase a *hyperbolic non-Abelian semimetal*.

Model.—HBT suggests a way to translate higher-dimensional Euclidean models to the hyperbolic plane. The mapping is especially lucid in the case of 4D Euclidean Hamiltonians because of a one-to-one correspondence between the Euclidean BZ and the hyperbolic U(1)-BZ of the $\{8, 8\}$ lattice. Motivated by this connection, we study the hyperbolic counterpart of the 4D quantum Hall insulator (QHI). Conventionally, the 4D Euclidean QHI is defined by a Dirac tight-binding model on the hypercubic lattice [44, 45]:

$$\mathcal{H} = \sum_{r,j} \left[\psi_r^\dagger \frac{\mathbb{F}_5 - i\mathbb{F}_j}{2} \psi_{r+j} + \text{h.c.} \right] + m \sum_r \psi_r^\dagger \mathbb{F}_5 \psi_r, \quad (1)$$

where \mathbb{F}_μ ($\mu=1, \dots, 5$) denote the five Dirac matrices satisfying the Clifford algebra $\{\mathbb{F}_\mu, \mathbb{F}_\nu\} = 2\delta_{\mu\nu}\mathbb{1}$. In terms of the Pauli matrices σ_i , the choice $\{\mathbb{F}_\mu\}_{\mu=1}^5 = \{\sigma_1\sigma_0, \sigma_2\sigma_0, \sigma_3\sigma_1, \sigma_3\sigma_2, \sigma_3\sigma_3\}$ ensures that \mathbb{F}_μ is real (imaginary) for μ odd (even). The four components of the spinor ψ_r correspond to internal/orbital degrees of freedom at site $r \in \mathbb{Z}^4$, and $j = 1, \dots, 4$ label orthogonal directions.

The $\{8, 8\}$ hyperbolic lattice, illustrated on the Poincaré disk in Fig. 1(a), provides a convenient setting to reinterpret the above model [15]. The notation $\{8, 8\}$ signifies that eight regular octagons meet at each vertex. Formally, the lattice is defined by its Fuchsian group Γ , an infinite translation group with four noncommuting generators γ_j [arrows in Fig. 1(a)] that obey a single constraint [37]:

$$\Gamma = \langle \gamma_1, \gamma_2, \gamma_3, \gamma_4 \mid \gamma_1\gamma_2^{-1}\gamma_3\gamma_4^{-1}\gamma_1^{-1}\gamma_2\gamma_3^{-1}\gamma_4 = 1 \rangle. \quad (2)$$

The ‘hyperbolized’ 4D QHI Hamiltonian is realized on the Poincaré disk with the following reinterpretation: r is the unit cell position on the complex plane and $r+j$ denotes a cell shifted by the translation operator γ_j .

In order to obtain a reciprocal-space perspective, we proceed in two steps. First, as in the Euclidean case, the lattice needs to be compactified, i.e., periodic boundary conditions (PBC) are imposed and edges of the unit cell related by translation symmetry are identified to produce a surface of genus $g \geq 2$ [37]. Unlike the Euclidean case, choosing an enlarged n -site unit cell ($n > 1$) increases the genus [43]. Second, one has to choose a d -dimensional IR D_λ of the translation group, where λ labels a point in a $[2d^2(g-1)+2]$ -dimensional space of d -dimensional IRs [38]. A generic Bloch Hamiltonian

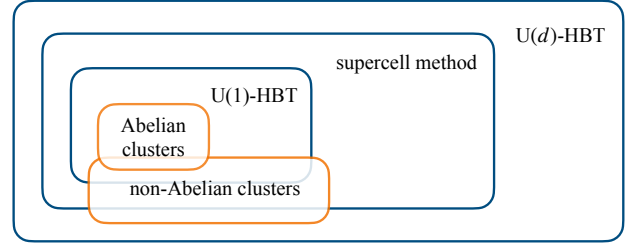


FIG. 2. Schematic summary of techniques used in this work to access eigenstates of hyperbolic lattices. Orange and blue denote real- and reciprocal-space methods, respectively. U(d) hyperbolic band theory ($d \geq 1$) encompasses all possible states.

$H_\lambda^{(n,d)}$ thus obtained determines the states in the Brillouin zone $\text{BZ}^{(n,d)}$. As we shall see, n and d provide two handles to access different sectors of the hyperbolic reciprocal space.

On the $\{8, 8\}$ lattice, the smallest unit cell ($n=1$ or primitive cell) is given by the red octagon in Fig. 1(a). It compactifies to a $g=2$ surface when the opposite edges are identified. Further, in U(1) ($d=1$ or Abelian) representations, λ are the crystal momenta whose components correspond to the four non-contractible cycles of the genus-2 surface. The mapping $D_\lambda(\gamma_j) = D_k(\gamma_j) = e^{ik_j}$ satisfies the constraint in Eq. (2) and allows us to define the U(1) Bloch Hamiltonian

$$H_k^{(1,1)} = \sum_\mu d_k^\mu \mathbb{F}_\mu, \quad (3)$$

as a compactified version of Eq. (1), with $d_k^\mu = (\sin k_1, \sin k_2, \sin k_3, \sin k_4, m_k)$ and $m_k = m + \sum_j \cos k_j$. Evidently, these expressions are equivalent to the Fourier transform of the Hamiltonian in Eq. (1), such that U(1)-HBT reproduces results from the 4D Euclidean case. Namely, at half-filling, the model undergoes topological phase transitions at $|m|=0, 2, 4$, but is gapped otherwise with a non-vanishing C_2 [45], as depicted in the top panel of Fig. 1(b). However, as foreshadowed earlier, one should also account for $d > 1$ IRs of Γ . We first demonstrate the existence of ‘in-gap’ states by real-space diagonalization on PBC clusters, and then show that these states originate from non-Abelian reciprocal space using U(d)-HBT and the supercell method (Fig. 2).

PBC clusters.—A PBC cluster is a closed hyperbolic lattice formed by pairing the open edges of a finite-sized lattice [46]. Efficient construction of large PBC clusters can be achieved through computational methods in geometric group theory (Appendix A). Depending on the particular edge pairing, PBC clusters can be classified into two categories: Abelian or non-Abelian [38]. In Abelian clusters, the non-Abelian hyperbolic translation group Γ modulo the edge pairing becomes Abelian. In other words, the translation generators effectively commute on Abelian clusters, so the wavefunctions of a translationally invariant Hamiltonian must be 1D IRs of the translation group in Eq. (2). We exclusively consider non-Abelian PBC clusters because we are interested in the higher-dimensional IRs arising from the non-commutativity of the generators, and because such clusters are necessary to correctly approximate the ther-

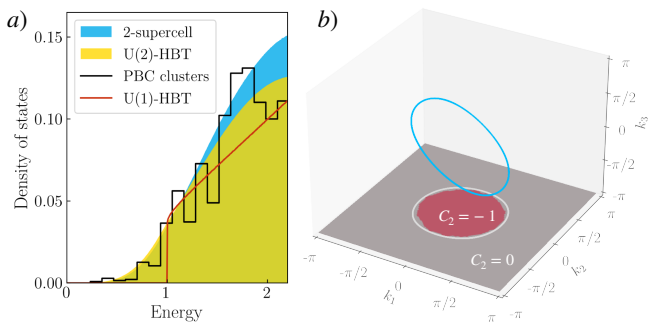


FIG. 3. Hyperbolic non-Abelian semimetal on the $\{8, 8\}$ lattice with Dirac mass $m = 3$. (a) Energy spectra from PBC clusters, $U(d)$ -HBT, and the supercell method. In contrast to the hard gap predicted by $U(1)$ -HBT, all three approaches indicate a semimetallic DOS that is symmetric about zero energy. (b) Low-energy excitations are manifested by a nodal ring in the 2-supercell description. Numerically obtained nodes in the 6D $BZ^{(2,1)}$ have been projected to the first three momentum components. Projection onto the first two coordinates appears as the grey curve. Computing the second Chern number C_2 as a function of (k_1, k_2) shows that 4D subspaces corresponding to points inside the ring are topological.

modynamic limit [40–43]. We numerically diagonalize the hyperbolized Hamiltonian (1) on 13 non-Abelian $\{8, 8\}$ PBC clusters, with the number of primitive cells ranging from 300 to 1800. The resulting DOS averaged over these clusters for $m = 3$ is depicted by the black curve in Fig. 3(a). Our first main finding is the discovery of states within the gap where no $U(1)$ Bloch states of $H_{\mathbf{k}}^{(1,1)}$ exist.

U(d)-HBT.—To demonstrate that these in-gap states can be attributed to non-Abelian Bloch physics, we first describe the corresponding BZs. Here, the Bloch states transform in representations $D_{\lambda}(\gamma_j) = U_j e^{ik_j}$, where $U = \{U_j\}_{j=1}^d \in SU(d)$ are special unitary ($d \times d$) matrices that satisfy Eq. (2). The specification of λ requires $2d^2 + 2$ parameters, of which four may be understood as hyperbolic momenta $\mathbf{k} = \{k_j\}_{j=1}^d$ and the remaining $2d^2 - 2$ characterize U [38]. Focusing on a single primitive cell ($n = 1$), the states in $BZ^{(1,d)}$ can be described by the non-Abelian Bloch Hamiltonian

$$H_{\lambda}^{(1,d)} = \sum_j \left[\left(\frac{\mathbb{I}_5 - i\mathbb{I}_j}{2} \right) \otimes D_{\lambda}(\gamma_j) + \text{h.c.} \right] + m (\mathbb{I}_5 \otimes \mathbb{1}_d). \quad (4)$$

Higher-dimensional IRs introduce an additional d -fold degeneracy in the associated Bloch states. Although an explicit parameterization of $BZ^{(1,d)}$ is currently lacking, as outlined in Appendix B, one may instead randomly sample the subspace of $SU(d)$ matrices that obey Eq. (2). For different choices of U and \mathbf{k} , a numerical diagonalization of $H_{\lambda}^{(1,d)}$ allows for a reconstruction of the $U(d)$ spectra. The DOS thus obtained for the simplest class of non-Abelian Bloch states, $d = 2$ IRs, is plotted together with the $U(1)$ DOS in Fig. 3(a). Consistent with our exact diagonalization results on PBC clusters, non-Abelian states fill the band gap of the Abelian spectrum.

Supercell method.—An alternative way to access non-Abelian Bloch states is the supercell method [43]. Instead of tessellating

the infinite lattice with copies of the primitive cell [red octagon in Fig. 1(a)], the lattice is subdivided into collections of $n > 1$ primitive cells, called n -supercells [blue polygon in Fig. 1(a) depicts the 2-supercell]. Copies of primitive cells covering the lattice are related to each other by elements of the full translation group of the lattice $\Gamma^{(1)} = \Gamma$, while copies of the 2-supercells, say, are related only by elements of a normal subgroup $\Gamma^{(2)}$ of $\Gamma^{(1)}$.

In either case, translation symmetry allows a single-cell description of the infinite system by going to hyperbolic reciprocal space as described previously. In Euclidean lattices, enlarging the unit cell introduces band folding and a reduction in BZ size such that the total number of states remains constant. In contrast, in the hyperbolic case the decomposition of reciprocal space into the generalized BZs is changed: The BZs for the primitive cell, $BZ^{(1,d)}$, are different from the ones for the 2-supercell, $BZ^{(2,d)}$. Nevertheless, their union (over IR dimensions d) is expected to remain the same, such that both are descriptions of the same infinite system.

As a consequence of the negative curvature, the genus g of the compactified manifold, and thereby the dimension of $BZ^{(n,1)}$, which is a $2g$ -dimensional torus, grows linearly with the supercell size n (Appendix C). In particular, $BZ^{(1,1)}$ is 4D, while $BZ^{(2,1)}$ is 6D. The advantage of working with supercells comes from the fact that, in contrast to the non-Abelian BZs, the $U(1)$ -BZs are well-understood and an explicit parametrization in terms of Bloch phase factors is known. Due to $\Gamma^{(2)}$ being a subgroup of $\Gamma^{(1)}$, some states in $BZ^{(2,1)}$ can be interpreted as non-Abelian states with respect to the translation group associated with the primitive cell, i.e., states in $BZ^{(1,d)}$ for $d > 1$ [43]. This implies that by applying $U(1)$ -HBT to larger supercells, more non-Abelian states can be captured.

Using the HYPERCELLS package [47], we find that $U(1)$ -HBT on the 2-supercell confirms our earlier findings: a semimetallic DOS within the gap of $U(1)$ -HBT on the primitive cell. This is demonstrated in Appendix C by computing the DOS for a sequence of supercells [43, 48] and observing rapid convergence near zero energy.

Nodal ring.—In unison, the three methods used so far paint a clear picture: While the $U(1)$ spectrum is gapped, non-Abelian Bloch states render the system semimetallic. Since the DOS near zero energy is well approximated by the 2-supercell, we derive an approximate low-energy theory by studying the Bloch Hamiltonian $H_{\mathbf{k}}^{(2,1)}$ analytically for $|m| \geq 3$. We find that its zero-energy eigenstates form a nodal ring inside $BZ^{(2,1)}$ whose projection onto a 3D subspace is shown in Fig. 3(b). Furthermore, this nodal ring is protected by inversion and time-reversal symmetries (Appendix F). Through a basis change of the Hamiltonian, linear transformation of momentum components from \mathbf{k} to $\tilde{\mathbf{k}}$ and a Taylor expansion of $H_{\tilde{\mathbf{k}}}^{(2,1)}$ in small momenta \mathbf{q} around the origin (see Appendix D), one can show that the spectral gap vanishes when

$$q_1^2 + q_2^2 = 6(4 - |m|). \quad (5)$$

The nodal manifold lies entirely in the (q_1, q_2) plane and, as a circle with mass-dependent radius, it shrinks to a point at the topological phase transitions $|m| = 4$. To understand the nodal

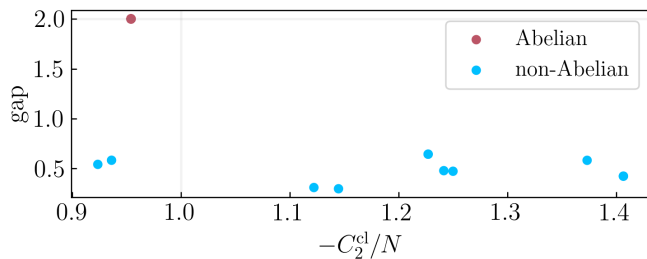


FIG. 4. Flux insertion in PBC clusters. We study Abelian and non-Abelian clusters with $N = 16, 18, 20$ primitive cells and use a phase space grid of 20^4 to compute the cluster second Chern number C_2^{cl} with $m = 3$. While the Abelian clusters agree with U(1)-HBT, non-Abelian clusters show smaller gaps owing to the semimetallic states and C_2^{cl}/N has a larger variance.

topology, it is useful to draw parallels with Weyl semimetals in 3D Euclidean space.

Weyl nodes can be understood as sources and sinks of Berry curvature in momentum space. As a consequence of the dipolar configuration, a 2D plane situated between two nodes of opposite charge experiences a net Berry flux and features a finite Chern number. Figure 1(c) pictures the scenario where the 2D planes are orthogonal to the vector joining the Weyl nodes. In a similar spirit, one may expect the nodal ring in 6D hyperbolic reciprocal space to encode nontrivial topology. Since our starting point was the 4D QHI, the second Chern number C_2 [49] is the relevant topological quantity. Indeed, integration over the four momenta k_3, k_4, k_5, k_6 shows that the nodal ring projection to the k_1, k_2 plane encloses a region where $C_2 = -1$, as shown in Fig. 3(c).

While the DOS of 3D Weyl semimetals near $E = 0$ scales as $\rho(E) \propto E^2$ [2], we expect that for the hyperbolic non-Abelian semimetal it scales as $\rho(E) \propto E^4$. To see this, first observe that the tight-binding Hamiltonian \mathcal{H} carries a spinful space-time-inversion symmetry, $\mathcal{PT} = \mathbb{F}_2 \mathbb{F}_4 \mathcal{K}$ with $(\mathcal{PT})^2 = -\mathbb{1}$ (\mathcal{K} is complex conjugation), inherited from the 4D QHI [45]. The \mathcal{PT} symmetry also descends to the Bloch Hamiltonians $H_{\mathbf{k}}^{(n,d)}$. It follows from the von Neumann-Wigner theorem [50, 51] that $H_{\mathbf{k}}^{(n,d)}$ generically exhibits band nodes of codimension $\mathfrak{d} = 5$, consistent with the observed nodal ring of dimension $\dim[\text{BZ}^{(2,1)}] - \mathfrak{d} = (6 - 5) = 1$. Generically, we expect the bands to disperse linearly in the five directions perpendicular (\perp) to the nodal ring, implying the DOS scaling $\rho(E) = \int d^5 k_{\perp} \delta(E - v|k_{\perp}|) \propto E^4$. Through numerical analysis (Appendix E), we corroborate that the DOS scales as $\rho(E) \propto E^{\alpha}$, where α varies with m within the range (3.3, 4.2).

Experimental signatures.—A priori, any physical realization of a hyperbolic lattice has states that transform under higher-dimensional IRs. To experimentally probe non-Abelian states, however, one needs to isolate them from the U(1) states. The hyperbolic non-Abelian semimetal provides an energy window to *exclusively* access these states. In coplanar waveguide resonators [11], for instance, a gap would appear as a dip in the transmission spectra, whereas a finite DOS at low energies would support transmission.

To understand the physical implications of nodal topology, recall the case of Weyl semimetals. There, each 2D slice between the Weyl nodes, carrying nonzero value of C_1 [cf. Fig. 1(c)], contributes to anomalous Hall conductance $\sigma_{xy} = (e^2/2\pi h) \Delta k$ where Δk is the momentum node separation [2–4]. Similarly, the response of the hyperbolic non-Abelian semimetal to external fields should be contingent on the nodal manifold geometry. We therefore study the second Chern number C_2^{cl} in small PBC clusters (consisting of N primitive cells), which is generated by filled states under flux insertion $(\mathbb{F}_5 - i\mathbb{F}_j) \mapsto (\mathbb{F}_5 - i\mathbb{F}_j)e^{i\phi_j}$ with $\phi \in [0, 2\pi)^{\times 4}$ in Eq. (1) (see Appendix G). Practically, such phase manipulation can be implemented with tunable complex-phase elements [12] in topoelectrical circuits [13–15], where the eigenstates necessary for computing C_2^{cl} can be accessed with simple oscilloscope measurements. For Abelian states, the flux insertion induces a momentum shift $\mathbf{k} \mapsto \mathbf{k} + \phi$; therefore, all eigenstates contribute equally to the integration, implying $C_2^{\text{cl}}/N = C_2$. In contrast, the trajectory of non-Abelian states under flux insertion may fall outside the nodal-ring manifold [cf. Fig. 3(b)], or pass through an additional nodal manifold not represented in the 6D BZ^(2,1). In both cases, one anticipates deviation from the linear scaling $C_2^{\text{cl}} = NC_2$. Figure 4 (supplemented with further data in Appendix G) shows the result of such integration for randomly selected Abelian (red) and non-Abelian (blue) clusters, revealing agreement with our theoretical arguments. We leave the study of the convergence of C_2^{cl}/N in the thermodynamic limit [40–43] to future works.

Conclusion.—Semimetals are fertile platforms that emulate particle physics models on the one hand and actualize solid-state notions of topology on the other. Conventionally, they have been studied in Euclidean space. Extending the notion of topological band nodes to negatively curved space, we investigated the hyperbolized 4D QHI Hamiltonian. The model exhibits striking features that have no counterpart in Euclidean crystals, such as band nodes stabilized by a second Chern number and low-energy excitations transforming exclusively in non-Abelian IRs of the hyperbolic translation group.

Our findings motivate broader and more systematic studies of band topology in hyperbolic lattices. In particular, the semimetallic nature of the hyperbolized QHI model inspires the search for fully gapped hyperbolic models characterized by a finite second Chern number [20]. Further research avenues are suggested by investigating parallels of the hyperbolic non-Abelian semimetal with 3D Weyl semimetals; such as potential analogs of the Nielsen-Ninomiya doubling theorem [52], and whether such doubling can be avoided [45, 53] on the surface of a 3D hyperbolic insulator with Kleinian symmetry group [54, 55]. On the experimental front, to probe the non-linear transport associated with C_2 [44], one needs to reconcile a dimensionality mismatch: the hyperbolic plane is two-dimensional, whereas four orthogonal directions enter (via the four-component Levi-Civita symbol) the non-linear response to applied fields [45, 56]. In a broader context, exciting open questions arise for hyperbolic topological models in relation to the bulk-boundary correspondence [16–18] and the holographic principle [57–60].







Acknowledgements.—We would like to thank I. Boettcher and R. Thomale for valuable discussions. T. T. and T. N. acknowledge funding from the European Research Council (ERC)

under the European Union’s Horizon 2020 research and innovation programm (ERC-StG-Neupert-757867-PARATOP). A. C. was supported by the University of Alberta startup fund UOFAB Startup Boettcher and the Avadh Bhatia Fellowship. J. M. was supported by NSERC Discovery Grants #RGPIN-2020-06999 and #RGPAS-2020-00064; the Canada Research Chair (CRC) Program; the Government of Alberta’s Major Innovation Fund (MIF); the Tri-Agency New Frontiers in Research Fund (NFRF, Exploration Stream); and the Pacific Institute for the Mathematical Sciences (PIMS) Collaborative Research Group program. P. M. L. and T. B. were supported by the Ambizione grant No. 185806 by the Swiss National Science Foundation (SNSF). T. B. was supported by the Starting Grant No. 211310 by SNSF.

-
- [1] X. Wan, A. M. Turner, A. Vishwanath, and S. Y. Savrasov, Topological semimetal and Fermi-arc surface states in the electronic structure of pyrochlore iridates, *Phys. Rev. B* **83**, 205101 (2011).
- [2] A. A. Zyuzin and A. A. Burkov, Topological response in Weyl semimetals and the chiral anomaly, *Phys. Rev. B* **86**, 115133 (2012).
- [3] P. Hosur and X. Qi, Recent developments in transport phenomena in Weyl semimetals, *C. R. Phys.* **14**, 857 (2013).
- [4] A. A. Burkov, Anomalous Hall Effect in Weyl Metals, *Phys. Rev. Lett.* **113**, 187202 (2014).
- [5] M. M. Vazifeh and M. Franz, Electromagnetic Response of Weyl Semimetals, *Phys. Rev. Lett.* **111**, 027201 (2013).
- [6] O. Vafek and A. Vishwanath, Dirac Fermions in Solids: From High- T_c Cuprates and Graphene to Topological Insulators and Weyl Semimetals, *Annu. Rev. Condens. Matter Phys.* **5**, 83 (2014).
- [7] N. P. Armitage, E. J. Mele, and A. Vishwanath, Weyl and Dirac semimetals in three-dimensional solids, *Rev. Mod. Phys.* **90**, 015001 (2018).
- [8] N. P. Ong and S. Liang, Experimental signatures of the chiral anomaly in Dirac–Weyl semimetals, *Nat. Rev. Phys.* **3**, 394 (2021).
- [9] H. Gao, J. W. Venderbos, Y. Kim, and A. M. Rappe, Topological Semimetals from First Principles, *Annu. Rev. Mater. Sci.* **49**, 153 (2019).
- [10] Coxeter, H. S. M., Crystal symmetry and its generalizations, *Proc. Trans. R. Soc. Can.* **51**, 1 (1957).
- [11] A. J. Kollár, M. Fitzpatrick, and A. A. Houck, Hyperbolic lattices in circuit quantum electrodynamics, *Nature* **571**, 45 (2019).
- [12] A. Chen, H. Brand, T. Helbig, T. Hofmann, S. Imhof, A. Fritzsche, T. Kießling, A. Stegmaier, L. K. Upreti, T. Neupert, T. Bzdušek, M. Greiter, R. Thomale, and I. Boettcher, Hyperbolic matter in electrical circuits with tunable complex phases, *Nat. Commun.* **14**, 622 (2023).
- [13] P. M. Lenggenhager, A. Stegmaier, L. K. Upreti, T. Hofmann, T. Helbig, A. Vollhardt, M. Greiter, C. H. Lee, S. Imhof, H. Brand, T. Kießling, I. Boettcher, T. Neupert, R. Thomale, and T. Bzdušek, Simulating hyperbolic space on a circuit board, *Nat. Commun.* **13**, 4373 (2022).
- [14] W. Zhang, H. Yuan, N. Sun, H. Sun, and X. Zhang, Observation of novel topological states in hyperbolic lattices, *Nat. Commun.* **13**, 2937 (2022).
- [15] W. Zhang, F. Di, X. Zheng, H. Sun, and X. Zhang, Hyperbolic band topology with non-trivial second Chern numbers, *Nat. Commun.* **14**, 1083 (2023).
- [16] S. Yu, X. Piao, and N. Park, Topological Hyperbolic Lattices, *Phys. Rev. Lett.* **125**, 053901 (2020).
- [17] D. M. Urwyler, P. M. Lenggenhager, I. Boettcher, R. Thomale, T. Neupert, and T. Bzdušek, Hyperbolic Topological Band Insulators, *Phys. Rev. Lett.* **129**, 246402 (2022).
- [18] Z.-R. Liu, C.-B. Hua, T. Peng, and B. Zhou, Chern insulator in a hyperbolic lattice, *Phys. Rev. B* **105**, 245301 (2022).
- [19] Q. Pei, H. Yuan, W. Zhang, and X. Zhang, Engineering boundary-dominated topological states in defective hyperbolic lattices, *Phys. Rev. B* **107**, 165145 (2023).
- [20] A. Chen, Y. Guan, P. M. Lenggenhager, J. Maciejko, I. Boettcher, and T. Bzdušek, Symmetry and topology of hyperbolic Haldane models, *arXiv:2304.03273* (2023).
- [21] K. Ikeda, S. Aoki, and Y. Matsuki, Hyperbolic band theory under magnetic field and Dirac cones on a higher genus surface, *J. Phys.: Condens. Matter* **33**, 485602 (2021).
- [22] A. Stegmaier, L. K. Upreti, R. Thomale, and I. Boettcher, Universality of Hofstadter Butterflies on Hyperbolic Lattices, *Phys. Rev. Lett.* **128**, 166402 (2022).
- [23] A. J. Kollár, M. Fitzpatrick, P. Sarnak, and A. A. Houck, Line-Graph Lattices: Euclidean and Non-Euclidean Flat Bands, and Implementations in Circuit Quantum Electrodynamics, *Commun. Math. Phys.* **376**, 1909 (2020).
- [24] A. Saa, E. Miranda, and F. Rouxinol, Higher-dimensional Euclidean and non-Euclidean structures in planar circuit quantum electrodynamics, *arXiv:2108.08854* (2021).
- [25] T. Bzdušek and J. Maciejko, Flat bands and band-touching from real-space topology in hyperbolic lattices, *Phys. Rev. B* **106**, 155146 (2022).
- [26] R. Mosseri, R. Vogeler, and J. Vidal, Aharonov-Bohm cages, flat bands, and gap labeling in hyperbolic tilings, *Phys. Rev. B* **106**, 155120 (2022).
- [27] Z.-R. Liu, C.-B. Hua, T. Peng, R. Chen, and B. Zhou, Higher-order topological insulators in hyperbolic lattices, *Phys. Rev. B* **107**, 125302 (2023).
- [28] Y.-L. Tao and Y. Xu, Higher-order topological hyperbolic lattices, *Phys. Rev. B* **107**, 184201 (2023).
- [29] J. Sun, C.-A. Li, S. Feng, and H. Guo, Hybrid higher-order skin-topological effect in hyperbolic lattices, *arXiv:2305.19810* (2023).
- [30] X. Zhu, J. Guo, N. P. Breuckmann, H. Guo, and S. Feng, Quantum phase transitions of interacting bosons on hyperbolic lattices, *J. Phys.: Condens. Matter* **33**, 335602 (2021).
- [31] P. Bienias, I. Boettcher, R. Belyansky, A. J. Kollár, and A. V. Gorshkov, Circuit Quantum Electrodynamics in Hyperbolic Space: From Photon Bound States to Frustrated Spin Models, *Phys. Rev. Lett.* **128**, 013601 (2022).
- [32] N. Gluscevich, A. Samanta, S. Manna, and B. Roy, Dynamic mass generation on two-dimensional electronic hyperbolic lattices, *arXiv:2302.04864* (2023).
- [33] N. Gluscevich and B. Roy, Magnetic catalysis in weakly interacting hyperbolic Dirac materials, *arXiv:2305.11174* (2023).
- [34] H. Yan, Hyperbolic fracton model, subsystem symmetry, and holography, *Phys. Rev. B* **99**, 155126 (2019).
- [35] H. Yan, K. Slagle, and A. H. Nevidomskyy, Y-cube model and fractal structure of subdimensional particles on hyperbolic lattices, *arXiv:2211.15829* (2022).
- [36] I. Boettcher, A. V. Gorshkov, A. J. Kollár, J. Maciejko, S. Rayan, and R. Thomale, Crystallography of hyperbolic lattices, *Phys. Rev. B* **105**, 125118 (2022).
- [37] J. Maciejko and S. Rayan, Hyperbolic band theory, *Sci. Adv.* **7**, abe9170 (2021).
- [38] J. Maciejko and S. Rayan, Automorphic Bloch theorems for

- hyperbolic lattices, *Proc. Natl. Acad. Sci. U.S.A.* **119** (2022).
- [39] N. Cheng, F. Serafin, J. McInerney, Z. Rocklin, K. Sun, and X. Mao, Band Theory and Boundary Modes of High-Dimensional Representations of Infinite Hyperbolic Lattices, *Phys. Rev. Lett.* **129**, 088002 (2022).
- [40] F. R. Lux and E. Prodan, Spectral and Combinatorial Aspects of Cayley-Crystals, [arXiv:2212.10329](https://arxiv.org/abs/2212.10329) (2023).
- [41] F. R. Lux and E. Prodan, Converging Periodic Boundary Conditions and Detection of Topological Gaps on Regular Hyperbolic Tessellations, [arXiv:2303.15611](https://arxiv.org/abs/2303.15611) (2023).
- [42] R. Mosseri and J. Vidal, Density of states of tight-binding models in the hyperbolic plane, [arXiv:2304.02382](https://arxiv.org/abs/2304.02382) (2023).
- [43] P. M. Lenggenhager, J. Maciejko, and T. Bzdušek, Non-Abelian hyperbolic band theory from supercells, [arXiv:2305.04945](https://arxiv.org/abs/2305.04945) (2023).
- [44] S.-C. Zhang and J. Hu, A Four-Dimensional Generalization of the Quantum Hall Effect, *Science* **294**, 823 (2001).
- [45] X.-L. Qi, T. L. Hughes, and S.-C. Zhang, Topological field theory of time-reversal invariant insulators, *Phys. Rev. B* **78**, 195424 (2008).
- [46] F. Sausset and G. Tarjus, Periodic boundary conditions on the pseudosphere, *J. Phys. A: Math. Theor.* **40**, 12873 (2007).
- [47] P. M. Lenggenhager, J. Maciejko, and T. Bzdušek, HYPERCELLS package (2023), (to be released soon).
- [48] M. Conder, [Quotients of triangle groups acting on surfaces of genus 2 to 101](https://arxiv.org/abs/0708.101) (2007).
- [49] M. Mochol-Grzelak, A. Dauphin, A. Celi, and M. Lewenstein, Efficient algorithm to compute the second Chern number in four dimensional systems, *Quantum Sci. Technol.* **4**, 014009 (2018).
- [50] J. von Neumann and E. Wigner, Über das Verhalten von Eigenwerten bei adiabatischen Prozessen, *Phys. Z.* **30**, 465 (1929).
- [51] T. Bzdušek and M. Sigrist, Robust doubly charged nodal lines and nodal surfaces in centrosymmetric systems, *Phys. Rev. B* **96**, 155105 (2017).
- [52] H. Nielsen and M. Ninomiya, The Adler-Bell-Jackiw anomaly and Weyl fermions in a crystal, *Phys. Lett. B* **130**, 389 (1983).
- [53] M. Creutz, Aspects of chiral symmetry and the lattice, *Rev. Mod. Phys.* **73**, 119 (2001).
- [54] W. P. Thurston, Three dimensional manifolds, Kleinian groups and hyperbolic geometry, *Bull. Am. Math. Soc.* **6**, 357 (1982).
- [55] D. Mumford, C. Series, and D. Wright, *Indra's Pearls: The Vision of Felix Klein* (Cambridge University Press, Cambridge, England, 2002).
- [56] H. M. Price, O. Zilberberg, T. Ozawa, I. Carusotto, and N. Goldman, Four-Dimensional Quantum Hall Effect with Ultracold Atoms, *Phys. Rev. Lett.* **115**, 195303 (2015).
- [57] E. Witten, Anti-de Sitter space and holography, *Adv. Theor. Math. Phys.* **2**, 253 (1998).
- [58] J. Zaanen, Y.-W. Sun, Y. Liu, and K. Schalm, *Holographic Duality in Condensed Matter Physics* (Cambridge University Press, Cambridge, England, 2015).
- [59] M. Asaduzzaman, S. Catterall, J. Hubisz, R. Nelson, and J. Unmuth-Yockey, Holography on tessellations of hyperbolic space, *Phys. Rev. D* **102**, 034511 (2020).
- [60] J. Chen, F. Chen, Y. Yang, L. Yang, Z. Chen, Y. Meng, B. Yan, X. Xi, Z. Zhu, G.-G. Liu, P. P. Shum, H. Chen, R.-G. Cai, R.-Q. Yang, Y. Yang, and Z. Gao, Ads/CFT Correspondence in Hyperbolic Lattices (2023), [arXiv:2305.04862](https://arxiv.org/abs/2305.04862).
- [61] F. Rober, The GAP package LINS, <https://github.com/FriedrichRober/LINS> (2020).
- [62] GAP, *GAP – Groups, Algorithms, and Programming, Version 4.11.1*, The GAP Group (2021).
- [63] D. Firth, *An Algorithm to Find Normal Subgroups of a Finitely Presented Group, up to a Given Finite Index*, Ph.D. thesis, University of Warwick (2004).
- [64] D. J. S. Robinson, *A Course in the Theory of Groups*, 2nd ed. (Springer, New York, 1996).
- [65] Á. Nagy and S. Rayan, On the hyperbolic Bloch transform, *Ann. Henri Poincaré* (2023).
- [66] J. B. Bronzan, Parametrization of $SU(3)$, *Phys. Rev. D* **38**, 1994 (1988).
- [67] R. Miranda, *Algebraic Curves and Riemann Surfaces* (American Mathematical Society, Providence, 1995).
- [68] S. Ryu, A. P. Schnyder, A. Furusaki, and A. W. W. Ludwig, Topological insulators and superconductors: tenfold way and dimensional hierarchy, *New J. Phys.* **12**, 065010 (2010).

Supplementary Material for: Hyperbolic non-Abelian semimetal

Tarun Tummuru ^{1,*} Anffany Chen ^{2,3} Patrick M. Lenggenhager ^{1,4,5}
 Titus Neupert ¹ Joseph Maciejko ^{2,3} and Tomáš Bzdušek ^{1,4,†}

¹*Department of Physics, University of Zurich, Winterthurerstrasse 190, 8057 Zurich, Switzerland*

²*Theoretical Physics Institute, University of Alberta, Edmonton, Alberta T6G 2E1, Canada*

³*Department of Physics, University of Alberta, Edmonton, Alberta T6G 2E1, Canada*

⁴*Condensed Matter Theory Group, Paul Scherrer Institute, 5232 Villigen PSI, Switzerland*

⁵*Institute for Theoretical Physics, ETH Zurich, 8093 Zurich, Switzerland*

(Dated: July 20, 2023)

CONTENTS

| | |
|---|----|
| A. PBC clusters | 1 |
| 1. Large-index normal subgroups from intersection | 1 |
| 2. Adjacency matrix | 3 |
| 3. Hamiltonian construction | 3 |
| B. $U(d)$ -HBT | 3 |
| C. Supercell method | 4 |
| D. 2-supercell Bloch Hamiltonian | 6 |
| E. Mass dependence of the nodal manifold | 7 |
| F. Symmetry-protected nodal ring | 7 |
| G. Flux insertion in PBC clusters | 10 |

Appendix A: PBC clusters

PBC clusters are finite-sized hyperbolic lattices with periodic boundary conditions (PBC). Owing to the spatial curvature, applying PBC to a finite $\{p, q\}$ hyperbolic lattice is a nontrivial task relying on geometric group theory [38, 40, 41, 46]. In this section, we describe our method for constructing PBC clusters, which applies to $\{p, q\}$ lattices with known hyperbolic Bravais lattices and corresponding unit cells [12, 20, 36]. The hyperbolic translation group Γ of a hyperbolic Bravais lattice is generated by elements γ_j which relate pairs of edges of the primitive cell. A PBC cluster with N primitive cells is defined by a choice of normal subgroup $\tilde{\Gamma} \triangleleft \Gamma$ of index N corresponding to a set of translations under which the wave function is invariant [38]. Given such a normal subgroup, one can compute the factor group $\Gamma/\tilde{\Gamma}$, which is a finite group of order N and corresponds to a group of translations modulo PBC on the finite cluster. The structure of the factor group allows us to construct an adjacency matrix A on the cluster, in which each lattice site corresponds to a coset $[\eta] \in \Gamma/\tilde{\Gamma}$. We use $[\eta]$ to denote the right coset of $\eta \in \Gamma$, i.e., $[\eta] = \tilde{\Gamma}\eta = \{\tilde{\eta}\eta : \tilde{\eta} \in \tilde{\Gamma}\}$. More complicated tight-binding models—with multiple on-site degrees

of freedom (e.g., orbitals or sublattices)—can then be built by tensoring the adjacency matrix A with finite-dimensional matrices in orbital/sublattice space. PBC clusters with Abelian factor group $\Gamma/\tilde{\Gamma}$ are termed Abelian clusters, and such clusters exclude all higher-dimensional IRs of the translation group. To study the gapless spectrum of the hyperbolic non-Abelian semimetal, we focus on non-Abelian clusters, whose factor group is non-Abelian and allows us to discretely sample the spectrum of non-Abelian Bloch states.

In the following, we outline our methodology for constructing the tight-binding Dirac model on *arbitrarily large* non-Abelian PBC clusters of the $\{8, 8\}$ hyperbolic (Bravais) lattice, with hyperbolic translation group Γ defined in Eq. (2). Appendix A 1 presents a method based on subgroup intersection to overcome the computational limitations of Ref. [38], in which only modest system sizes $N \leq 25$ had been reached. The algorithm to construct the adjacency matrix A on a PBC cluster is explained in Appendix A 2. Finally, in Appendix A 3, we construct the Hamiltonian for the hyperbolized QHI model.

1. Large-index normal subgroups from intersection

In Ref. [38], a GAP implementation [61, 62] of the low-index normal subgroups procedure [63] was used to enumerate all normal subgroups $\tilde{\Gamma}$ up to a given finite index N_{\max} . Such a procedure is computationally expensive, and Ref. [38] only presented results for PBC clusters of maximum size $N_{\max} = 25$. To overcome these limitations, we propose an algorithm based on a few mathematical results. First, given two normal subgroups $\tilde{\Gamma}^{(1)}, \tilde{\Gamma}^{(2)}$ of the Fuchsian translation group Γ , we show that their intersection $\tilde{\Gamma}^{(1)} \cap \tilde{\Gamma}^{(2)}$ is also normal in Γ and thus defines a valid PBC cluster. In the following, we denote set inclusion by \subseteq , subgroup inclusion by \leq , and normal subgroup inclusion by \triangleleft .

Lemma A.1. *Let $H, K \triangleleft G$. Then $H \cap K \triangleleft G$.*

Proof. First, we prove that $H \cap K \leq G$. If $g, h \in H \cap K$, they are also in H . Since H is a group, then $gh \in H$. On the other hand, g, h are also in K , and since K is also a group, we have $gh \in K$. Since gh is both in H and in K , we have $gh \in H \cap K$. But this holds for every pair of elements g, h in $H \cap K$, thus $H \cap K$ is a group. Since $H \cap K$ is contained in G as a set, it is a subgroup of G .

Next, we prove that $H \cap K$ is normal in G . Consider an element b of the set $g(H \cap K)$. Since H contains $H \cap K$, it

* tarun.tummuru@uzh.ch

† tomas.bzusek@uzh.ch

is also true that $b \in gH$, and since K also contains $H \cap K$, it is also true that $b \in gK$. Therefore, b must belong to the intersection $gH \cap gK$. Since this is true for any $b \in g(H \cap K)$, we have $g(H \cap K) \subseteq gH \cap gK$. However, we can also show that the converse is true: $gH \cap gK \subseteq g(H \cap K)$. Let $b \in gH \cap gK$. Then, $b \in gH$ and $b \in gK$, and there exist $h \in H$ and $k \in K$ such that $b = gh = gk$. Multiplying by g^{-1} , we find that $h = k \in H \cap K$. Thus, $b \in g(H \cap K)$, and since b was otherwise arbitrary, we find that $gH \cap gK \subseteq g(H \cap K)$. Since both $g(H \cap K) \subseteq gH \cap gK$ and $gH \cap gK \subseteq g(H \cap K)$ are true, we necessarily have that $g(H \cap K) = gH \cap gK$. We leave it as an exercise to the reader to also prove using exactly the same arguments that $(H \cap K)g = Hg \cap Kg$.

We finally show that the latter two equalities imply normality of $H \cap K$ in G . Let $g \in G$, then $H \triangleleft G$ implies $gH = Hg$, and $K \triangleleft G$ implies $gK = Kg$. Therefore, $g(H \cap K) = gH \cap gK = Hg \cap Kg = (H \cap K)g$, thus $H \cap K \triangleleft G$. \square

Next, we show that the index of $\tilde{\Gamma}^{(1)} \cap \tilde{\Gamma}^{(2)}$ is bounded from below by the least common multiple of the indices of $\tilde{\Gamma}^{(1)}$ and $\tilde{\Gamma}^{(2)}$, and is thus typically larger than either individual index.

Lemma A.2. *Let $H, K \triangleleft G$ with indices $|G : H| = m$ and $|G : K| = n$. Then*

$$\text{lcm}(m, n) \leq |G : H \cap K| \leq mn, \quad (\text{A1})$$

with the equality (i.e., $|G : H \cap K| = mn$) realized for m, n coprime.

Proof. First, observe that $H \cap K$ is a subgroup of both H and K , since it is a group and is contained in both H and K . Since $H \cap K \leq H \leq G$, we have (see 1.3.5 in Ref. [64])

$$|G : H \cap K| = |G : H| |H : H \cap K| = m |H : H \cap K|. \quad (\text{A2})$$

Also, $H \cap K \leq K \leq G$, thus

$$|G : H \cap K| = |G : K| |K : H \cap K| = n |K : H \cap K|. \quad (\text{A3})$$

Hence $|G : H \cap K|$ is a common multiple of m and n , thus $|G : H \cap K| \geq \text{lcm}(m, n)$. For the second inequality in Eq. (A1), see 1.3.11(ii) in Ref. [64]; it becomes an equality for m, n coprime (and $\text{lcm}(m, n) = mn$ in that case). \square

Finally, we show that the intersection of normal subgroups $\tilde{\Gamma}^{(1)}$ and $\tilde{\Gamma}^{(2)}$ corresponding to Abelian clusters can only produce another Abelian cluster. To accomplish this, we rely on the notion of commutator subgroup. The commutator subgroup of a group is generated by all commutators of the group elements. Roughly speaking, the commutator subgroup is a measure of non-commutativity: a large commutator subgroup indicates a ‘less Abelian’ group.

Lemma A.3. *Let $H \triangleleft G$. Then G/H is Abelian if and only if H contains the commutator subgroup $[G, G] = \langle [g_1, g_2] | g_1, g_2 \in G \rangle$.*

Proof. Denote the (right) coset of $g_1 \in G$ by $[g_1] = Hg_1$. Using the normality of H in G , we have:

$$[g_1][g_2] = (Hg_1)(Hg_2) = H(g_1Hg_1^{-1})g_1g_2 = Hg_1g_2. \quad (\text{A4})$$

Likewise, $[g_2][g_1] = Hg_2g_1$. Assume that G/H is Abelian, then $[g_1][g_2] = [g_2][g_1]$, which implies $Hg_1g_2 = Hg_2g_1$. Multiplying by $(g_2g_1)^{-1} = g_1^{-1}g_2^{-1}$ from the right, we obtain $H[g_1, g_2] = H$ where $[g_1, g_2] = g_1g_2g_1^{-1}g_2^{-1}$ is the commutator of g_1 and g_2 . This implies that $[g_1, g_2] \in H$ for all $g_1, g_2 \in G$, thus $[G, G] \subseteq H$.

Now instead, assume $[G, G] \subseteq H$. For any $g_1, g_2 \in G$, we have:

$$\begin{aligned} [g_1][g_2] &= Hg_1g_2 = Hg_1g_2(g_1^{-1}g_2^{-1}g_2g_1) = H[g_1, g_2]g_2g_1 \\ &= Hg_2g_1 = [g_2][g_1], \end{aligned} \quad (\text{A5})$$

hence G/H is Abelian. We have used $H[g_1, g_2] = H$ which holds since $[g_1, g_2] \in [G, G] \subseteq H$. \square

Theorem A.4. *Let $H, K \triangleleft G$. Then G/H and G/K are both Abelian if and only if $G/(H \cap K)$ is Abelian.*

Proof. First assume that G/H and G/K are Abelian. By Lemma A.3, $[G, G]$ is contained in both H and K . Thus $[G, G] \subseteq H \cap K$, and by the same Lemma, $G/(H \cap K)$ is Abelian. Now assume instead that $G/(H \cap K)$ is Abelian. By the same Lemma, $[G, G]$ is contained in $H \cap K$, and thus is contained in both H and K . As a result, G/H and G/K are both Abelian. \square

Thus, for a cluster constructed from subgroup intersection to be non-Abelian, it is a necessary and sufficient condition that at least one of the two clusters in the intersection is non-Abelian.

We now describe the computational procedure for generating normal subgroups of Γ . We begin with the list of small-index normal subgroups generated by the methods of Ref. [38]. We then randomly select n_p parent subgroups $\{\tilde{\Gamma}^{(p)}\}_{p=1}^{n_p}$ among this list with indices between N_{\min} and N_{\max} , keeping only the ones with non-Abelian factor groups. We then compute in GAP the intersection

$$\tilde{\Gamma}^\cap \equiv \bigcap_{p=1}^{n_p} \tilde{\Gamma}^{(p)} \quad (\text{A6})$$

of the parent subgroups. (Using Lemma A.1 repeatedly, it is clear that $\tilde{\Gamma}^\cap$ thus constructed is normal in Γ for any n_p .)

If the factor group $\Gamma/\tilde{\Gamma}^\cap$ is of sufficiently large order (i.e., system size), we construct the adjacency matrix for the corresponding non-Abelian PBC cluster. To obtain normal subgroups within some target index range, we have experimented with the input parameters $(n_p, N_{\min}, N_{\max})$. We find that input parameters $(n_p, N_{\min}, N_{\max}) = (2, 15, 20)$ result in $\tilde{\Gamma}^\cap$ with indices $N \sim 300$, while $(n_p, N_{\min}, N_{\max}) = (3, 10, 15)$ gives indices $N \sim 1500\text{--}2000$. For our analysis, we randomly chose 13 normal subgroups $\tilde{\Gamma}^\cap$ with indices $N = \{304, 304, 320, 320, 306, 1560, 1584, 1716, 1800, 1800, 1872, 1980, 1980\}$, which correspond to the sizes of PBC clusters [see Fig. S1(a)]. The 1D IRs make up 1/2 of all eigenstates in the first four clusters, while the fraction is 1/3 in the other clusters. Note that such indices are completely out of reach of brute-force applications of the low-index normal subgroups procedure, as done e.g. in Refs. [25, 38]. By contrast, the method presented here can, in principle, produce normal subgroups of arbitrarily large indices.

2. Adjacency matrix

We employ GAP [62] to construct an adjacency matrix A from a previously obtained normal subgroup $\tilde{\Gamma}^\cap$ with a large index N . If two elements $[\eta_n], [\eta_m] \in \Gamma/\tilde{\Gamma}^\cap$ correspond to nearest neighbors, they must be related by one of the generators γ_j of Γ [38]:

$$[\eta_n] = [\eta_m][\gamma_j]. \quad (\text{A7})$$

Here, we include $\{\gamma_1, \gamma_2, \gamma_3, \gamma_4\}$ and their inverses in the generating set:

$$\{\gamma_j\}_{j=1}^8 \equiv \{\gamma_1, \gamma_2, \gamma_3, \gamma_4, \gamma_1^{-1}, \gamma_2^{-1}, \gamma_3^{-1}, \gamma_4^{-1}\}. \quad (\text{A8})$$

The algorithm proceeds through the following steps:

1. Compute the factor group $\Gamma/\tilde{\Gamma}^\cap$.
2. Compute the right cosets of generators $\{\gamma_j\}_{j=1}^8$:
 - (a) Construct the homomorphism $\Phi : \Gamma \rightarrow \Gamma/\tilde{\Gamma}^\cap$ which sends each element $\eta \in \Gamma$ to the right coset $[\eta] = \tilde{\Gamma}^\cap \eta$.
 - (b) Compute the right coset $[\gamma_j] = \Phi(\gamma_j)$ for $j = 1, \dots, 8$.
3. Construct the adjacency matrix A :
 - (a) Initialize A as an $N \times N$ matrix with zero entries.
 - (b) For each pair of elements $[\eta_n], [\eta_m] \in \Gamma/\tilde{\Gamma}^\cap$, if $[\eta_n] = [\eta_m][\gamma_j]$ for some integer $j \in [1, 8]$, then $[\eta_n]$ and $[\eta_m]$ are nearest neighbors and we let $A_{nm} \rightarrow A_{nm} + 1$. Note that it is possible to have $A_{nm} \geq 1$, implying that there are multiple generators relating $[\eta_n]$ and $[\eta_m]$. This is uncommon for large clusters.
4. Construct a matrix B to record the indices of all the generators that relate a given pair of neighbors:
 - (a) Initialize B as a three-dimensional $N \times N \times 8$ array with zero entries.
 - (b) For each pair of elements $[\eta_n], [\eta_m] \in \Gamma/\tilde{\Gamma}^\cap$ and for each index $j \in [1, 8]$, if $[\eta_n] = [\eta_m][\gamma_j]$, then let $B_{n,m,j} = 1$; otherwise let $B_{n,m,j} = 0$.

Step 4 is required for implementing additional on-site degrees of freedom (e.g., orbitals or sublattices), as in the Dirac model (see Appendix A 3).

3. Hamiltonian construction

The Dirac model on a $\{8, 8\}$ PBC cluster with N sites is described by a $4N \times 4N$ Hamiltonian matrix H . A 4-component spinor ψ lives on each site. Nearest-neighboring spinors are coupled by inter-site matrices

$$T_j = \frac{\mathbb{F}_5 - i\mathbb{F}_j}{2}, \text{ for } j = 1, \dots, 4, \quad (\text{A9})$$

and their Hermitian conjugates,

$$T_j = T_{j-4}^\dagger = \frac{\mathbb{F}_5 + i\mathbb{F}_{j-4}}{2}, \text{ for } j = 5, \dots, 8, \quad (\text{A10})$$

where $\mathbb{F}_\mu = (\mathbb{F}_\mu)^\dagger$ with $\mu = 1, \dots, 5$ are the Dirac matrices. Given the adjacency matrix A and the generator-label matrix B of a PBC cluster, the procedure for defining the Dirac model is as follows:

1. Initialize H as a $4N \times 4N$ matrix with zero entries.
2. For each pair of neighboring sites n and m such that $A_{nm} > 0$, use matrix B to recall the indices of the generators that relate sites n and m . For each recalled index j' , add to H the tensor product of M , which is a $N \times N$ matrix with zeros everywhere except at $M_{nm} = 1$, and $T_{j'}$:

$$H \rightarrow H + M \otimes T_{j'}. \quad (\text{A11})$$

3. To add a nonzero mass m , add to H the tensor product of the identity matrix $I_{N \times N}$ and \mathbb{F}_5 :

$$H \rightarrow H + mI_{N \times N} \otimes \mathbb{F}_5. \quad (\text{A12})$$

The DOS for H thus constructed is shown for various PBC clusters and compared with $U(1)$ -HBT in Fig. S1(a).

Appendix B: $U(d)$ -HBT

Here we provide details about the algorithm for sampling $BZ^{(1,d)}$. We focus on the simplest class of non-Abelian Bloch states, i.e., $(d=2)$ -dimensional irreducible representations, where the matrices U_j , $j = 1, \dots, 4$ belong to the $SU(2)$ group. In Fig. S1(b), the data for $SU(3)$ are obtained by nearly identical steps, with the only difference being the matrix dimension and parameterization.

In general, an $SU(2)$ matrix may be parameterized as

$$U_j = \begin{pmatrix} a_j & b_j \\ -b_j^* & a_j^* \end{pmatrix}, \quad (\text{B1})$$

where $a_j, b_j \in \mathbb{C}$ and $|a_j|^2 + |b_j|^2 = 1$. The latter condition reduces the number of free real parameters to three. To be a valid representation of the Fuchsian group Γ , one has to ensure that the choice of four matrices U obey

$$U_1 U_2^{-1} U_3 U_4^{-1} U_1^{-1} U_2 U_3^{-1} U_4 - \mathbb{1}_2 = 0. \quad (\text{B2})$$

The procedure to find solutions $\{U_j\}_{j=1}^4 \equiv U$ is as follows. We pick random $U_{1,2}$ according to the circular unitary ensemble, which represents a uniform distribution over the unitary $d \times d$ matrices, and corresponds to the Haar measure on the unitary group. Subsequently, we choose a random initial choice of $U_{3,4}$ according to the same uniform distribution, which we decompose into $a_{3,4}$ and $b_{3,4}$ per Eq. (B1), and we perform a gradient descent with respect to these parameters to minimize the Frobenius norm of Eq. (B2). Sometimes, this procedure

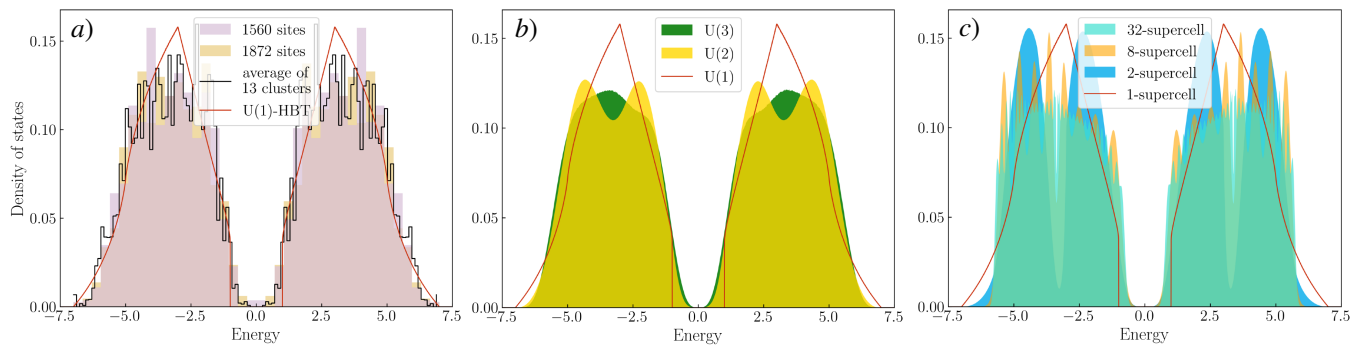


FIG. S1. A comparison of different techniques to access non-Abelian Bloch states in the hyperbolic QHI model at $m = 3$. (a) Sample DOS of two PBC clusters, alongside the average of 13 clusters (120 bins). (b) $U(d)$ -HBT for $d = 1, 2$ and 3 . While $U(1)$ -HBT is gapped, spectra of higher-dimensional IRs are semimetallic. (c) Going beyond the 2-supercell, we observe that the spectra tend to converge in the limit of large supercells.

gets trapped in a local minimum that does not solve Eq. (B2); in that case the matrices are discarded and we repeat the steps for a different choice of fixed $U_{1,2}$ and initial $U_{3,4}$. The algorithm is iterated until we reach a specified number of random solutions U .

To motivate why our described approach for finding random representations U works, let us discuss the dimensions of the mathematical spaces at play. First, the space of *distinct* d -dimensional (unitary) representations D_λ of Γ , i.e., where equivalent representations are treated as a single point, is called the $U(d)$ -character variety $X(\Sigma_2, U(d))$; here, Σ_2 is the genus-2 surface obtained from compactifying the edges of the primitive cell of the $\{8, 8\}$ lattice. This variety is known to be ten-dimensional [38, 65]. One can further decompose the representation matrices on the group generators as $D_\lambda(\gamma_j) = U_j e^{ik_j}$, where $e^{ik_j} \in U(1)$ and $U_j \in SU(2)$. The $U(1)$ factors clearly absorb four of the ten dimensions of $X(\Sigma_2, U(2))$, implying that the space of non-equivalent $SU(2)$ representation matrices that obey Eq. (B2) is six-dimensional.

Crucially, in our numerical search for random $SU(2)$ matrices obeying Eq. (B2) we also need to account for distinct choices of representation matrices U that fall into the same equivalence class. Recall that given a unitary matrix M , the choice MUM^\dagger constitutes a representation of Γ that is *equivalent* to U as it merely corresponds to a unitary rotation of the eigenvectors of the Hamiltonian $H_\lambda^{(1,d)}$ that span the representation. However, our numerical search is not restricted from potentially finding equivalent representations. Since the $SU(2)$ group is three-dimensional, the orbit $\cup_{M \in SU(2)} MUM^\dagger$ of the set $\{U_j\}_{j=1}^4$ is generically three-dimensional; consequently, such unitary transformations increase the extent of $SU(2)$ solutions U to Eq. (B2) to a nine-dimensional manifold. By selecting a randomly chosen $U_{1,2}$, we fix six of the nine parameters; in other words, the space of solutions for $U_{3,4}$ with given $U_{1,2}$ (if such solutions exist) is generically three-dimensional. We verified that by performing minimization of the Frobenius norm of Eq. (B2) for different initial choices of $U_{3,4}$ and fixed $U_{1,2}$ we obtain different optimized solutions for $U_{3,4}$. Note that finding solutions for U_4 given randomly chosen $U_{1,2,3}$, which corresponds to fixing nine coordinates, generically does *not*

yield any result. This is because the orbit of a single matrix $\cup_{M \in SU(2)} MUM^\dagger$ can be shown to be only two-dimensional. As a consequence, fixing three random matrices $U_{1,2,3}$ already overdetermines the problem of finding U_4 .

Before concluding, let us make three final remarks. First, to make sure that we investigate all *dimensions* of $BZ^{(1,d)}$ uniformly, we compute the Hamiltonian spectrum for $L^6 \times L^4 = L^{10}$ unitary representations; here, L^6 points correspond to the random choice of $SU(2)$ matrices U inside the six-dimensional space of distinct representations, and L^4 corresponds to choices of $U(1)$ factors $\{e^{ik_j}\}_{j=1}^4$ inside the four-dimensional space of momenta. For the presented data, we chose $L = 8$. Second, owing to the lack of explicit parametrizations of these higher BZs, it is presently unknown to us whether they are equipped with a canonical measure of volume. Therefore, it is possible that our random sampling is non-homogeneous, i.e., it explores some sectors more densely than others. Despite these subtleties, the good agreement of $U(2)$ -HBT and 2-supercell DOS lends support to the outlined scheme. Finally, when generalizing the algorithm to $SU(3)$ matrices, the decomposition in Eq. (B1) has to be replaced by an eight-parameter decomposition, as shown in Ref. [66]. A comparison of DOS computed from randomly sampled 2D and 3D representations is shown in Fig. S1(b).

We note in passing that while $U(d)$ -HBT on the primitive cell and $U(1)$ -HBT on n -supercells provide complementary ways to access the non-Abelian states, an investigation of $U(d)$ Bloch theory on n -supercells could conceivably open up a larger share of the hyperbolic reciprocal space.

Appendix C: Supercell method

As described in the main text, the supercell method [43] applies $U(1)$ -HBT to supercells in order to gain access to the non-Abelian BZs. By considering sequences of supercells with increasing number n of primitive cells, an increasing number of non-Abelian Bloch states is generated and convergence is achieved for $n \rightarrow \infty$. Supercells can be defined [43] in terms of factor groups G of the underlying space group (more precisely its proper subgroup) with a translation group Γ . The proper

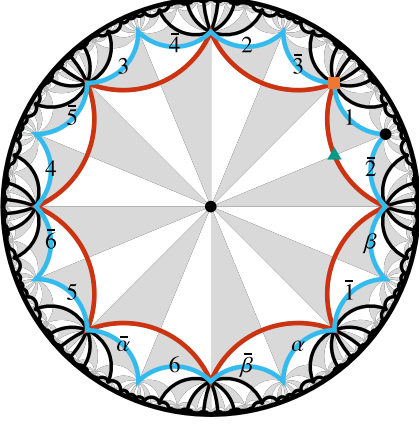


FIG. S2. Symmetries and unit cells of the $\{8, 8\}$ lattice. The space group symmetries of the lattice are illustrated by grey and white triangles which are generated by applying those symmetry operations to a single one of them. Both the symmetric primitive cell (red polygon) as well as the symmetric 2-supercell (blue polygon) consisting of two copies of the primitive cell are shown. The boundary identification of the supercell is indicated as follows: the edge labeled \bar{j} is related to the edge labeled j by the translation generator $\gamma_j \in \Gamma^{(2)}$. Edges related by composite translations are labeled by $\bar{\alpha}$, $\alpha = \gamma_3^{-1}\gamma_1^{-1}$, and $\bar{\beta}$, $\beta = \gamma_4^{-1}\gamma_2^{-1}$. For the purpose of Appendix F, we indicate the following high-symmetry positions. Black dots mark inversion centers with respect to sites of the $\{8, 8\}$ lattice, green triangle with respect to mid-edge, and orange square with respect to faces of the lattice.

subgroup of the space group of the $\{8, 8\}$ lattice is the proper triangle group with presentation

$$\Delta^+(2, 8, 8) = \langle x, y, z \mid x^2, y^8, z^8, xyz \rangle, \quad (\text{C1})$$

generated by rotations x , y , and z around the three vertices of a hyperbolic triangle by angles $\frac{2\pi}{2}$, $\frac{2\pi}{8}$, and $\frac{2\pi}{8}$, respectively, which satisfy the constraints that the products listed after the vertical line are equal to the identity (Fig. S2).

To achieve convergence to the thermodynamic limit [40, 42], the sequence of translation groups $\Gamma^{(n)} \triangleleft \Delta^+$ needs to obey the normal subgroup relations

$$\Gamma^{(1)} \triangleright \Gamma^{(2)} \triangleright \dots \triangleright \Gamma^{(n)} \triangleright \dots, \quad (\text{C2})$$

$$\begin{aligned} \iota: \quad & \text{BZ}^{(1,1)} \rightarrow \text{BZ}^{(2,1)} \\ & (k_1, k_2, k_3, k_4) \mapsto (k_4 + k_1, k_2 - k_1, k_3 - k_2, k_4 - k_3, -k_4 - k_1, k_1 - k_2) \end{aligned} \quad (\text{C5})$$

Note that the immersion ι is not one-to-one (i.e., it is non-injective): two four-momenta that differ by π in all components $\{k_j\}_{j=1}^4$ are mapped onto the same six-momentum in $\text{BZ}^{(2,1)}$. This two-to-one mapping (associated with doubling of the number of bands) is analogous to the Brillouin-zone folding that accompanies supercell constructions in Euclidean lattices.

such that $\bigcap_{n \geq 1} \Gamma^{(n)}$ is the trivial group containing only the identity element [40]. The n -supercell is compactified into a surface of genus $g^{(n)}$ that grows linearly with n , as expressed by the Riemann-Hurwitz formula [67]. Specifically, if g_{pc} is the genus of the compactified primitive cell, then $g^{(n)} = n(g_{\text{pc}} - 1) + 1$. Here, we adopt the same sequence that was considered in Ref. [43] for the nearest-neighbor hopping model on the $\{8, 8\}$ lattice. This sequence was obtained from the factor groups given in Ref. [48] using the HYPERCELLS package [47] and they are denoted by T2.6, T3.11, T5.13, T9.20, T17.29, T33.44, where “Tg.j” labels the j^{th} quotient of any triangle group $\Delta^+(r, q, p)$ where the quotient acts on a surface of genus g . Their explicit presentations are

$$\begin{aligned} G^{(1)} &= \langle x, y, z \mid x^2, y^8, z^8, xyz, xzy, y^3z^{-1} \rangle, \\ G^{(2)} &= \langle x, y, z \mid x^2, y^8, z^8, xyz, xzy \rangle, \\ G^{(3)} &= \langle x, y, z \mid x^2, y^8, z^8, xyz, xy^{-2}z^{-1}y, xzy^{-1}z^{-2} \rangle, \\ G^{(4)} &= \langle x, y, z \mid x^2, y^8, z^8, xyz, xy^{-2}z^{-1}y \rangle, \\ G^{(5)} &= \langle x, y, z \mid x^2, y^8, z^8, xyz, xzy^{-2}z^{-2}y, (yz^{-1}y^2)^2 \rangle, \\ G^{(6)} &= \langle x, y, z \mid x^2, y^8, z^8, xyz, xzy^{-2}z^{-2}y \rangle. \end{aligned} \quad (\text{C3})$$

The 2-supercell derived from $G^{(2)}$ including boundary identifications is illustrated in Fig. S2. For each n -supercell, we construct the U(1) Bloch Hamiltonian $H_{\mathbf{k}}^{(n,1)}$, parameterized by the momentum vector $\mathbf{k} \in \text{BZ}^{(n,1)} \cong \mathbb{T}^{2g^{(n)}}$.

Because of the subgroup relations in Eq. (C2), one can always express supercell translation generators in terms of $\{\gamma_1, \gamma_2, \gamma_3, \gamma_4\}$ and their inverses. For the 2-supercell, specifically, we find

$$\begin{aligned} \tilde{\gamma}_1 &= \gamma_4\gamma_1, & \tilde{\gamma}_2 &= \gamma_1^{-1}\gamma_2, \\ \tilde{\gamma}_3 &= \gamma_2^{-1}\gamma_3, & \tilde{\gamma}_4 &= \gamma_3^{-1}\gamma_4, \\ \tilde{\gamma}_5 &= \gamma_4^{-1}\gamma_1^{-1}, & \tilde{\gamma}_6 &= \gamma_1\gamma_2^{-1}. \end{aligned} \quad (\text{C4})$$

These relations among the translation generators imply the following immersion of the original 4D $\text{BZ}^{(1,1)}$ inside the 6D $\text{BZ}^{(2,1)}$:

By randomly sampling $\text{BZ}^{(n,1)}$ with 10^9 \mathbf{k} -points and diagonalizing $H_{\mathbf{k}}^{(n,1)}$ for each of them, we compute the energy spectrum. The DOS is then obtained with an energy resolution of 0.005 [Fig. S1(c)]. The appearance of peaks in the DOS may be understood as a consequence of “band folding”, which increases the number of energy bands. We observe convergence

with increasing supercell size n . Crucially, the DOS near zero energy converges rapidly, such that already the 2-supercell (T3.11) gives a good approximation. Therefore, we next study the corresponding Bloch Hamiltonian $H_{\mathbf{k}}^{(2,1)}$ on the 6D BZ $^{(2,1)}$.

Appendix D: 2-supercell Bloch Hamiltonian

The Bloch Hamiltonian corresponding to the 2-supercell can be expressed as a linear combination of 8×8 matrices as

$$H_{\mathbf{k}}^{(2,1)} = \frac{1}{4} \sum_{ij\ell} d_{ij\ell} \sigma_{ij\ell}, \quad (\text{D1})$$

where $\sigma_{ij\ell} = \sigma_i \otimes \sigma_j \otimes \sigma_\ell$, with $\{\sigma_i\}_{i=0}^3$ denoting the Pauli matrices and the 2×2 identity matrix. The non-zero summands in Eq. (D1) are

$$d_{0,3,3} = 4m, \quad (\text{D2a})$$

$$d_{1,1,0} = -ie^{-i(k_2+k_3+k_4+k_5)} \left(-1 + e^{2i(k_2+k_3+k_4+k_5)} \right), \quad (\text{D2b})$$

$$d_{1,2,0} = -ie^{-i(k_2+k_3+k_4+k_5+k_6)} \left(-1 + e^{i(k_3+k_4+k_5+k_6)} \right) \left(1 + e^{i(2k_2+k_3+k_4+k_5+k_6)} \right), \quad (\text{D2c})$$

$$d_{1,3,1} = ie^{-i(k_1+k_2+k_3+k_4+k_6)} \left(e^{ik_1} - e^{i(k_4+k_6)} \right) \left(e^{ik_1} + e^{i(2k_2+k_3+k_4+k_6)} \right), \quad (\text{D2d})$$

$$d_{1,3,2} = ie^{-i(k_1+k_2+k_3+k_4)} \left(e^{ik_1} + e^{i(k_2+k_3+k_4)} \right) \left(-1 + e^{i(k_1+k_2+k_3+k_4)} \right), \quad (\text{D2e})$$

$$\begin{aligned} d_{1,3,3} = & e^{-i(k_1+k_2+k_3+k_4+k_5+k_6)} \left(e^{ik_1} + e^{i(2k_1+k_3+k_5)} + e^{i(k_1+k_6)} + e^{i(k_1+k_5+k_6)} + e^{i(k_1+k_4+k_5+k_6)} \right. \\ & + e^{i(k_1+k_3+k_4+k_5+k_6)} + e^{i(k_2+k_3+k_4+k_5+k_6)} + 2e^{i(k_1+k_2+k_3+k_4+k_5+k_6)} + e^{i(2k_1+k_2+k_3+k_4+k_5+k_6)} \\ & + e^{i(k_1+2k_2+k_3+k_4+k_5+k_6)} + e^{i(k_1+2k_2+2k_3+k_4+k_5+k_6)} + e^{i(k_1+2k_2+2k_3+2k_4+k_5+k_6)} \\ & \left. + e^{i(k_1+2k_2+2k_3+2k_4+2k_5+k_6)} + e^{i(2k_2+k_3+2k_4+k_5+2k_6)} + e^{i(k_1+2(k_2+k_3+k_4+k_5+k_6))} \right), \end{aligned} \quad (\text{D2f})$$

$$d_{2,1,0} = -e^{-i(k_2+k_3+k_4+k_5)} \left(-1 + e^{i(k_2+k_3+k_4+k_5)} \right)^2, \quad (\text{D2g})$$

$$d_{2,2,0} = -e^{-i(k_2+k_3+k_4+k_5+k_6)} \left(-1 + e^{i(k_3+k_4+k_5+k_6)} \right) \left(-1 + e^{i(2k_2+k_3+k_4+k_5+k_6)} \right), \quad (\text{D2h})$$

$$d_{2,3,1} = e^{-i(k_1+k_2+k_3+k_4+k_6)} \left(e^{ik_1} - e^{i(k_4+k_6)} \right) \left(e^{i(2k_2+k_3+k_4+k_6)} - e^{ik_1} \right), \quad (\text{D2i})$$

$$d_{2,3,2} = e^{-i(k_1+k_2+k_3+k_4)} \left(e^{i(k_2+k_3+k_4)} - e^{ik_1} \right) \left(-1 + e^{i(k_1+k_2+k_3+k_4)} \right), \quad (\text{D2j})$$

$$\begin{aligned} d_{2,3,3} = & ie^{-i(k_1+k_2+k_3+k_4+k_5+k_6)} \left(e^{ik_1} + e^{i(2k_1+k_3+k_5)} + e^{i(k_1+k_6)} + e^{i(k_1+k_5+k_6)} + e^{i(k_1+k_4+k_5+k_6)} \right. \\ & + e^{i(k_1+k_3+k_4+k_5+k_6)} - e^{i(k_2+k_3+k_4+k_5+k_6)} + e^{i(2k_1+k_2+k_3+k_4+k_5+k_6)} - e^{i(k_1+2k_2+k_3+k_4+k_5+k_6)} \\ & - e^{i(k_1+2k_2+2k_3+k_4+k_5+k_6)} - e^{i(k_1+2k_2+2k_3+2k_4+k_5+k_6)} - e^{i(k_1+2k_2+2k_3+2k_4+2k_5+k_6)} \\ & \left. - e^{i(2k_2+k_3+2k_4+k_5+2k_6)} - e^{i(k_1+2(k_2+k_3+k_4+k_5+k_6))} \right). \end{aligned} \quad (\text{D2k})$$

As we shall see in the next section, symmetries constrain some of the nodes to lie in the $(k_a, k_b, -k_a, -k_b, k_a, k_b)$ plane for $k_{a,b} \in [-\pi, \pi)$. To obtain the low-energy spectrum in this plane and to simplify the expressions, we proceed in three steps:

1. A basis transformation on the Bloch Hamiltonian makes the structure of the ring manifest in the small momentum expansion: $\tilde{H}_{\mathbf{k}}^{(2,1)} = V_H H_{\mathbf{k}}^{(2,1)} V_H^\dagger$, with $V_H = \text{diag}(1, 1, 1, 1, r, r, r, r)$ and $r = e^{i(k_1-k_2)/2}$.

2. For a direct handle on the nodal plane, we perform a basis

rotation to obtain the Hamiltonian $\tilde{H}_{\tilde{\mathbf{k}}}^{(2,1)}$ where $\tilde{\mathbf{k}} = V_{\mathbf{k}} \mathbf{k}$ and

$$V_{\mathbf{k}} = \frac{1}{\sqrt{6}} \begin{pmatrix} \sqrt{2} & 0 & \sqrt{3} & 0 & -1 & 0 \\ 0 & \sqrt{2} & 0 & \sqrt{3} & 0 & -1 \\ -\sqrt{2} & 0 & \sqrt{3} & 0 & 1 & 0 \\ 0 & -\sqrt{2} & 0 & \sqrt{3} & 0 & 1 \\ \sqrt{2} & 0 & 0 & 0 & 2 & 0 \\ 0 & \sqrt{2} & 0 & 0 & 0 & 2 \end{pmatrix}. \quad (\text{D3})$$

Essentially, $V_{\mathbf{k}}$ provides an orthonormal basis where the

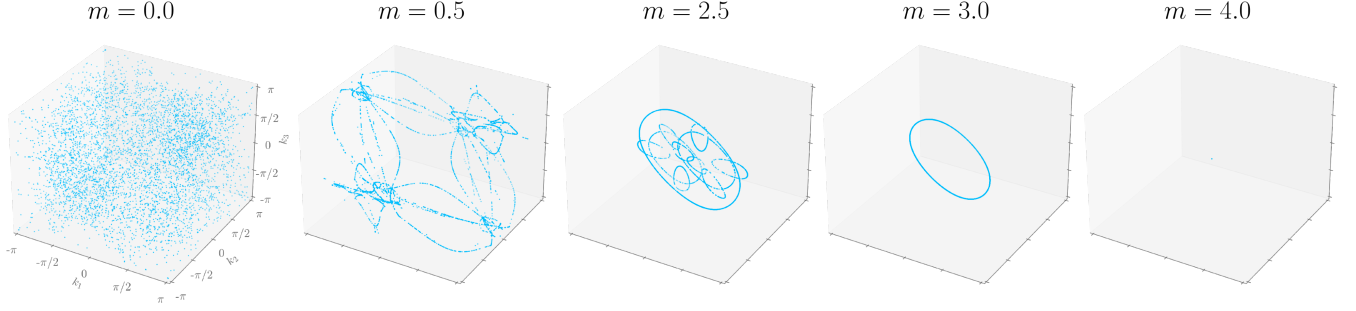


FIG. S3. Evolution of the nodal manifold of the 2-supercell as a function of mass m . Each point denotes a projected six-momentum coordinate where the spectral gap at half-filling vanishes. The nodal ring emerges close to $m = 3$, shrinks to a point at the origin when $m = 4$, and finally vanishes as the system enters the trivial insulating phase. The behavior is mirrored for negative values of the mass.

first two columns span the nodal plane and the ring now lies in $(\tilde{k}_1, \tilde{k}_2, 0, 0, 0, 0)$. At this stage, to leading order in momenta \mathbf{q} , the Hamiltonian near the origin is given by $\tilde{H}_{\mathbf{q}}^{(2,1)} = \sum_{ij\ell} d_{ij\ell} \sigma_{ij\ell}$ and

$$d_{0,3,3} = m, \quad (\text{D4a})$$

$$d_{1,3,3} = -\frac{q_1^2 + q_2^2}{6} + 4, \quad (\text{D4b})$$

$$d_{1,1,0} = \frac{q_3 + 2q_4 + \sqrt{3}q_5}{2\sqrt{2}}, \quad (\text{D4c})$$

$$d_{1,2,0} = \frac{q_3 + q_4 + \sqrt{3}(q_5 + q_6)}{2\sqrt{2}}, \quad (\text{D4d})$$

$$d_{1,3,1} = \frac{-2q_3 + q_4 + \sqrt{3}q_6}{2\sqrt{2}}, \quad (\text{D4e})$$

$$d_{1,3,2} = -\frac{q_3 + q_4}{\sqrt{2}}, \quad (\text{D4f})$$

$$d_{2,3,3} = \frac{3(q_3 + q_4) + \sqrt{3}(q_5 + q_6)}{\sqrt{2}}. \quad (\text{D4g})$$

Note that the nodal ring lies in the plane spanned by (q_1, q_2) and its form is apparent in $d_{1,3,3}$. The terms Eq. (D4)(b–f) form a set of mutually anti-commuting matrices. The eigenvalues in this low-energy approximation are given by

$$E^2 = \frac{1}{36} (q_1^2 + q_2^2 - 24)^2 + m^2 + X^2 + d_{2,3,3}^2 \quad (\text{D5})$$

$$\pm 2\sqrt{m^2 (d_{2,3,3}^2 + (q_1^2 + q_2^2 - 24)^2 / 36) + d_{2,3,3}^2 X^2},$$

wherein $X^2 = d_{1,1,0}^2 + d_{1,2,0}^2 + d_{1,3,1}^2 + d_{1,3,2}^2$ and each of the four energy bands is doubly degenerate.

3. To proceed, it would be convenient to diagonalize the expression X , i.e., identify an orthonormal basis for the coordinates (q_3, q_4, q_5, q_6) , while leaving (q_1, q_2) unaltered. By obtaining the eigenvectors of the matrix representation of X , it can be shown that with

$$\begin{pmatrix} q_3 \\ q_4 \\ q_5 \\ q_6 \end{pmatrix} \rightarrow \frac{1}{4} \begin{pmatrix} 2\alpha_+ & 2\beta_+ & 2\alpha_- & 2\beta_- \\ -\kappa_+ & \kappa_- & \kappa_- & \kappa_+ \\ \kappa_- & -\kappa_+ & \kappa_+ & \kappa_- \\ 2\alpha_- & -2\beta_- & -2\alpha_+ & 2\beta_+ \end{pmatrix} \begin{pmatrix} q_3 \\ q_4 \\ q_5 \\ q_6 \end{pmatrix}, \quad (\text{D6})$$

such that $\alpha_{\pm} = \sqrt{1 \pm \frac{1}{2\sqrt{19}}}$, $\beta_{\pm} = \sqrt{1 \pm \frac{7}{2\sqrt{19}}}$ and $\kappa_{\pm} = \sqrt{3} \pm 1$,

one has

$$4X^2 = (5 + \sqrt{19})q_3^2 + (3 + \sqrt{3})q_4^2 + (3 - \sqrt{3})q_5^2 + (5 - \sqrt{19})q_6^2. \quad (\text{D7})$$

From Eq. (D5), the energy vanishes when

$$4X^2 = -\left(\left(q_1^2 + q_2^2 \pm 24\right) / 6 \pm \sqrt{m^2 - d_{2,3,3}^2}\right)^2, \quad (\text{D8})$$

which in turn implies that $X = 0$, $q_3 = q_4 = q_5 = q_6 = 0$ and $d_{2,3,3} = 0$. It is then easy to deduce that the nodal line is described by $q_1^2 + q_2^2 = 6(4 - |m|)$.

Appendix E: Mass dependence of the nodal manifold

The nodal manifold of the 2-supercell in its 6D BZ can be further studied as a function of the mass m . As seen in Fig. S3, the manifold has a complicated structure when projected to the first three momentum coordinates. The simple structure of a nodal ring emerges only close to $m = 3$. Referring to the case of Weyl semimetals, the degeneracy in the spectrum can only be removed either by breaking translation symmetry and allowing the Weyl points to hybridize or by tuning model parameters to bring them together. Similarly, here the nodal ring shrinks to a point as one tunes the mass towards $m = 4$, which marks a phase transition to the trivial atomic limit. One can also extract the scaling of the DOS as a function of the energy and the results appear in Fig. S4. Exactly at $m = 0$, however, the 2-supercell DOS has a linear scaling that can be attributed to an additional symmetry and a change in the node co-dimension, as explained in Appendix F.

Appendix F: Symmetry-protected nodal ring

In this section, we analyze how certain crystalline symmetries of the hyperbolic $\{8, 8\}$ lattice impose particular band-structure features observed inside the 6D BZ^(2,1) of the 2-supercell Hamiltonian discussed in Appendix D. Special attention is given to space inversion (\mathcal{P}) and to time reversal (\mathcal{T}). In

particular, these symmetries allow us to address the three following aspects: (i) identify the 2D plane of the nodal ring, which is enforced by inversion of bands with opposite \mathcal{P} -inversion eigenvalues, (ii) clarify the two-fold Kramers degeneracy of all bands, and (iii) explain the codimension $\mathfrak{d} = 5$ for node formation at generic values of m as well as the significantly decreased codimension $\mathfrak{d} = 2$ observed for $m = 0$.

Let us begin by discussing the role of \mathcal{PT} symmetry in the 4D BZ $^{(1,1)}$ of the hyperbolic Bloch Hamiltonian $H_{\mathbf{k}}^{(1,1)}$ constructed on the primitive unit cell, which matches exactly the Bloch Hamiltonian of the 4D QHI on a hypercubic lattice [44, 45]. The topology of the latter Hamiltonian is well understood [68]. In particular, it is easily verified that $H_{\mathbf{k}}^{(1,1)}$ in Eq. (3) commutes with $\mathcal{PT} = \mathbb{F}_2 \mathbb{F}_4 \mathcal{K}$:

$$(\mathcal{PT})H_{\mathbf{k}}^{(1,1)}(\mathcal{PT})^{-1} = H_{\mathbf{k}}^{(1,1)} \quad (\text{F1})$$

where \mathbb{F}_2 and \mathbb{F}_4 are the two imaginary Dirac matrices. Since $(\mathcal{PT})^2 = -\mathbb{1}_4$, it follows that matrices $H_{\mathbf{k}}^{(1,1)}$ belong to the symplectic class [50], which corresponds to nodal class AII of Ref. [51]. Energy bands in this symmetry class exhibit two-fold Kramers degeneracies in the spectrum, while robust band degeneracies occurring at generic \mathbf{k} -points are of codimension $\mathfrak{d} = 5$ [50, 51] and therefore do not occur inside the 4D BZ $^{(1,1)}$.

On the other hand, robust point nodes may generically occur inside the five-dimensional space spanned by (\mathbf{k}, m) . Indeed, as manifested by the phase diagram in Fig. 1(b), topological phase transitions at $m \in \{0, \pm 2, \pm 4\}$ are facilitated through gap closings, which are pinned by inversion symmetry $\mathcal{P} = \mathbb{F}_5$ to high-symmetry momenta with components $\{k_j\}_{j=1}^4 \in \{0, \pi\}$:

$$\mathcal{P}H_{\mathbf{k}}^{(1,1)}\mathcal{P}^{-1} = H_{-\mathbf{k}}^{(1,1)}. \quad (\text{F2})$$

Since Dirac matrices \mathbb{F}_5 have eigenvalues ± 1 , each with multiplicity two, it follows from the $m_{\mathbf{k}}\mathbb{F}_5$ term in the Hamiltonian (3) that the consecutive topological phase transitions are driven by inversion of bands of opposite \mathcal{P} -eigenvalues at the various high-symmetry \mathbf{k} -points.

Let us remark that when representing the action of \mathcal{P} on the hyperbolic lattice in the coordinate space, we encounter certain non-uniqueness; namely, there are several distinct points of inversion center that are not related by symmetry of the $\{8, 8\}$ lattice. These inversion points respectively correspond to: vertices/sites (black dots in Fig. S2), mid-points of edges (green triangle in Fig. S2), and centers of faces (orange squares in Fig. S2) of the $\{8, 8\}$ lattice. Nevertheless, the inversion operations with respect to these distinct points belong to the same conjugacy class in the hyperbolic point group $G^{(1)} := \Delta^+/\Gamma^{(1)}$, where $\Delta^+ = \Delta^+(2, 8, 8)$ is the triangle group of the $\{8, 8\}$ lattice [36, 43] and $\Gamma^{(1)}$ is the translation group associated with the primitive unit cell. It follows that all the specified inversion centers transform the hyperbolic momentum in the same way, $\mathcal{P} : \mathbf{k} \mapsto -\mathbf{k}$, and each can, therefore, be interpreted as the coordinate-space equivalent of the inversion symmetry in Eq. (F2).

We next analyze how the notions of \mathcal{P} and \mathcal{T} symmetry, and of their composition \mathcal{PT} , generalize to the 6D BZ $^{(2,1)}$ associated with the hyperbolic Bloch Hamiltonian $H_{\mathbf{k}}^{(2,1)}$ on

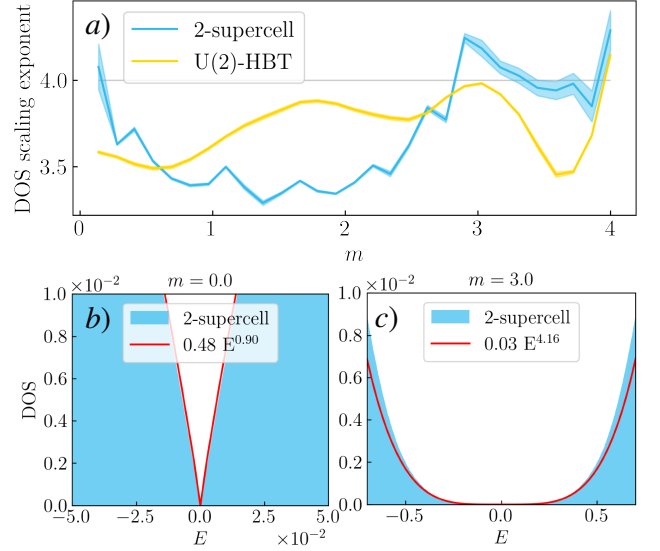


FIG. S4. (a) Low energy DOS scaling as function of m computed from U(2)-HBT and 2-supercell. The color filling around the curves represents the error estimate for the standard non-linear least squares fit. We use energies in the range $[0, 0.25]$ for the fit. The curves are shown in relation to predicted scaling of four from the Wigner-von Neumann argument. (b,c) DOS and best-fit curve for $m = 0$ resp. $m = 3$.

the 2-supercell, specified in Eqs. (D1–D2). Let us remind that a hyperbolic crystalline symmetry g transforms momentum components inside the 6D BZ $^{(2,1)}$ by a linear transformation $\mathbf{k} \mapsto \mathbf{k}' = M_g \cdot \mathbf{k}$, where we call $M_g \in \text{GL}(6, \mathbb{Z})$ the point-group matrix of g [20]. If g is a symmetry of the studied model, then the hyperbolic Bloch Hamiltonians $H_{\mathbf{k}}^{(2,1)}$ and $H_{\mathbf{k}'}^{(2,1)}$ are related by a linear (unitary or antiunitary) transformation, and consequently the energy spectra at \mathbf{k} and \mathbf{k}' are identical.

We first analyze the effect of time-reversal symmetry. Since \mathcal{T} does not act on spatial coordinates, it does not induce a non-trivial permutation of the boundaries of the 2-supercell. However, being an antiunitary operator, \mathcal{T} acts by complex conjugation on the twisted boundary conditions across the 2-supercell edges. The conjugation results in flipping the sign of all momentum components, implying $M_{\mathcal{T}} = -\mathbb{1}_6$, and there exists a unitary matrix $U_{\mathcal{T}}$ such that

$$H_{M_{\mathcal{T}}\cdot\mathbf{k}}^{(2,1)} = U_{\mathcal{T}} \cdot [H_{\mathbf{k}}^{(2,1)}]^* \cdot U_{\mathcal{T}}^\dagger \quad (\text{F3})$$

with the specific form of $U_{\mathcal{T}} = \sigma_0 \otimes (\mathbb{F}_1 \mathbb{F}_3) \mathcal{K}$.

In contrast to the primitive cell, the discussion of inversion symmetry for the 2-supercell branches into two cases; this is because the various choices of the inversion center now fall into *different* conjugacy classes in the (enlarged) point group $G^{(2)} := \Delta/\Gamma^{(2)}$, where $\Gamma^{(2)}$ is the (reduced) translation group of the 2-supercell. Specifically, the inversion \mathcal{P}^V with respect to vertices/sites (black dots in Fig. S2) and inversion \mathcal{P}^F with respect to centers of faces (orange square in Fig. S2) of the $\{8, 8\}$ lattice are *distinguished* from the inversion \mathcal{P}^E with respect to the mid-points of edges (green triangle in Fig. S2) of the $\{8, 8\}$ lattice. For this reason, to understand the full

implications of inversion symmetry on the spectrum of $H_{\mathbf{k}}^{(2,1)}$, one has to analyze the constraints imposed by both $\mathcal{P}^{\text{V,F}}$ and \mathcal{P}^{E} .

We begin by considering the inversion \mathcal{P}^{V} with respect to a vertex (which is equivalent to considering \mathcal{P}^{F}). By specifically taking the vertex in the center of the primitive cell, we recognize from the arrangement in Fig. S2 that \mathcal{P}^{V} permutes the subscripts of the translation generators as follows:

$$(1, 2, 3, 4, 5, 6, \alpha, \beta) \mapsto (5, 6, \alpha, \beta, 1, 2, 3, 4). \quad (\text{F4})$$

For 1D IRs, the relators among the eight generators of $\Gamma^{(2)}$ imply that $k_{\alpha} = -k_1 - k_3 - k_5$ and $k_{\beta} = -k_2 - k_4 - k_6$ [43], i.e., they are uniquely specified by the other six momentum components. Therefore, \mathcal{P}^{V} transforms momentum components as $\mathbf{k} \mapsto M_{\mathcal{P}^{\text{V}}} \cdot \mathbf{k}$ with

$$M_{\mathcal{P}^{\text{V}}} = \begin{pmatrix} 0 & 0 & 0 & 0 & 1 & 0 \\ 0 & 0 & 0 & 0 & 0 & 1 \\ -1 & 0 & -1 & 0 & -1 & 0 \\ 0 & -1 & 0 & -1 & 0 & -1 \\ 1 & 0 & 0 & 0 & 0 & 0 \\ 0 & 1 & 0 & 0 & 0 & 0 \end{pmatrix}. \quad (\text{F5})$$

We find that \mathcal{P}^{V} constraints the hyperbolic Bloch Hamiltonian for 2-supercell as

$$H_{M_{\mathcal{P}^{\text{V}}}\cdot\mathbf{k}}^{(2,1)} = U_{\mathcal{P}^{\text{V}},\mathbf{k}} \cdot H_{\mathbf{k}}^{(2,1)} \cdot U_{\mathcal{P}^{\text{V}},\mathbf{k}}^{\dagger}, \quad (\text{F6})$$

where

$$U_{\mathcal{P}^{\text{V}},\mathbf{k}} = \begin{pmatrix} 1 & 0 \\ 0 & e^{-i(k_2+k_3+k_4+k_5)} \end{pmatrix} \otimes \mathbb{F}_5. \quad (\text{F7})$$

We further identify \mathcal{P}^{V} -invariant momenta by solving for $\mathbf{k} \stackrel{\dagger}{=} M_{\mathcal{P}^{\text{V}}} \cdot \mathbf{k} \pmod{2\pi}$ in each of the six components), which defines two-dimensional planes

$$\mathcal{M}_{s_1, s_2} = \{(k_1, k_2, -k_1 + s_1, -k_2 + s_2, k_1, k_2) | \dots \\ \dots | k_{1,2} \in [-\pi, +\pi)\} \subset \text{BZ}^{(2,1)} \quad (\text{F8})$$

where $s_{1,2} \in \{0, \pi\}$. Within these planes, the exponential in Eq. (F7) evaluates to

$$e^{-i(k_2+k_3+k_4+k_5)}|_{\mathcal{M}_{s_1, s_2}} = e^{-i(s_1+s_2)} \in \{\pm 1\}, \quad (\text{F9})$$

and the eigenvalues of $U_{\mathcal{P}^{\text{V}}}$ within the high-symmetry planes are ± 1 , each with multiplicity four.

If inversion of bands with opposite \mathcal{P}^{V} eigenvalue occurs inside \mathcal{M}_{s_1, s_2} , then these bands are prevented from hybridization and a \mathcal{P}^{V} -protected nodal line is formed inside the plane \mathcal{M}_{s_1, s_2} . Crucially, as $|m|$ decreases across the critical value $|m_c| = 4$, band inversion occurs inside the 4D BZ of $H_{\mathbf{k}}^{(1,1)}$ at $\mathbf{k}^{(4\text{D})} = (0, 0, 0, 0)$ (for $m_c = -4$) resp. at $\mathbf{k}^{(4\text{D})} = (\pi, \pi, \pi, \pi)$ (for $m_c = +4$). Owing to the zone-folding of immersion ι in Eq. (C5), both four-momenta are mapped to the same six-momentum $\mathbf{k} = \mathbf{0}$ inside the plane $\mathcal{M}_{0,0}$. Therefore, we conclude that the topological transitions at $|m_c| = 4$ are associated with the formation of a nodal line inside the plane $\mathcal{M}_{0,0}$.

This prediction, rooted in symmetry analysis, agrees with the analytical calculation presented in Appendix D.

Next, we consider implications of the inversion \mathcal{P}^{E} with respect to the mid-point of an edge of the $\{8, 8\}$ lattice (green triangle in Fig. S2). To understand how \mathcal{P}^{E} acts on the momenta inside $\text{BZ}^{(2,1)}$, we use GAP [61, 62] to express conjugations $\mathcal{P}^{\text{E}}\tilde{\gamma}_j(\mathcal{P}^{\text{E}})^{-1}$ of the generators $\{\tilde{\gamma}_j\}_{j=1}^6$ of the translation group $\Gamma^{(2)}$ as composite words in $\{\tilde{\gamma}_j\}_{j=1}^6$ [20]. We obtain

$$\tilde{\gamma}_1 \mapsto \tilde{\gamma}_1^{-1}, \quad (\text{F10a})$$

$$\tilde{\gamma}_2 \mapsto \tilde{\gamma}_2^{-1}, \quad (\text{F10b})$$

$$\tilde{\gamma}_3 \mapsto \tilde{\gamma}_2\tilde{\gamma}_3^{-1}\tilde{\gamma}_2^{-1}, \quad (\text{F10c})$$

$$\tilde{\gamma}_4 \mapsto \tilde{\gamma}_2\tilde{\gamma}_3\tilde{\gamma}_4^{-1}\tilde{\gamma}_3^{-1}\tilde{\gamma}_2^{-1}, \quad (\text{F10d})$$

$$\tilde{\gamma}_5 \mapsto \tilde{\gamma}_2\tilde{\gamma}_3\tilde{\gamma}_4\tilde{\gamma}_5^{-1}\tilde{\gamma}_4^{-1}\tilde{\gamma}_3^{-1}\tilde{\gamma}_2^{-1}, \quad (\text{F10e})$$

$$\tilde{\gamma}_6 \mapsto \tilde{\gamma}_2\tilde{\gamma}_3\tilde{\gamma}_4\tilde{\gamma}_5^{-1}\tilde{\gamma}_1^{-1}\tilde{\gamma}_6^{-1}\tilde{\gamma}_4^{-1}\tilde{\gamma}_2^{-1}\tilde{\gamma}_1, \quad (\text{F10f})$$

which at the level of Abelian representations $\rho(\tilde{\gamma}_j) = e^{ik_j}$ simplifies to a diagonal point-group matrix $M_{\mathcal{P}^{\text{E}}} = -\mathbb{1}_6$. Since \mathcal{P}^{E} exchanges the two sites within the 2-supercell, we find that

$$H_{M_{\mathcal{P}^{\text{E}}}\cdot\mathbf{k}}^{(2,1)} = U_{\mathcal{P}^{\text{E}}} \cdot H_{\mathbf{k}}^{(2,1)} \cdot U_{\mathcal{P}^{\text{E}}}^{\dagger}, \quad (\text{F11})$$

where

$$U_{\mathcal{P}^{\text{E}}} = \sigma_1 \otimes \mathbb{F}_5. \quad (\text{F12})$$

Importantly, note that the composition $\mathcal{P}^{\text{E}}\mathcal{T}$ acts trivially on $\text{BZ}^{(2,1)}$:

$$M_{\mathcal{P}^{\text{E}}\mathcal{T}} = M_{\mathcal{P}^{\text{E}}} \cdot M_{\mathcal{T}} = \mathbb{1}_6, \quad (\text{F13})$$

while inside the Hilbert space of Bloch states at \mathbf{k} it acts by an antiunitary transformation:

$$U_{\mathcal{P}^{\text{E}}\mathcal{T}} = U_{\mathcal{P}^{\text{E}}} \cdot U_{\mathcal{T}} = \sigma_1 \otimes (\mathbb{F}_1\mathbb{F}_3)\mathcal{K}. \quad (\text{F14})$$

Since $(U_{\mathcal{P}^{\text{E}}\mathcal{T}})^2 = -\mathbb{1}_6$, we conclude that Hamiltonian matrices $H_{\mathbf{k}}^{(2,1)}$ belong to the symplectic class (nodal class AII of Ref. [51]) whose spectrum exhibits Kramers degeneracy and the band nodes are generically of codimension $\mathfrak{d} = 5$. This is consistent with the observed formation of $(6 - 5) = 1$ -dimensional nodal lines inside $\text{BZ}^{(2,1)}$, as illustrated with numerically extracted data in Fig. S3.

We finally tackle the particular case of $m = 0$, where Fig. S3 suggests a higher-dimensional nodal manifold, and Fig. S4 indicates an altered scaling of the density of states. For this choice of the mass parameter, an additional sublattice symmetry \mathcal{S} arises, which leaves the six-dimensional momentum \mathbf{k} invariant ($M_{\mathcal{S}} = \mathbb{1}_6$). It acts on the Hilbert space by a unitary matrix:

$$U_{\mathcal{S}} = \sigma_3 \otimes \mathbb{1}_4, \quad (\text{F15})$$

and that flips the sign of energy:

$$U_{\mathcal{S}} \cdot H_{\mathbf{k}}^{(2,1)} \cdot U_{\mathcal{S}}^{-1} = -H_{\mathbf{k}}^{(2,1)}. \quad (\text{F16})$$

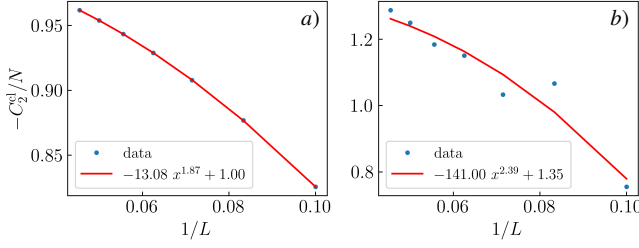


FIG. S5. Scaling of C_2^{cl}/N as a function of the linear mesh size L for (a) an Abelian and (b) a non-Abelian cluster with $N = 16$ primitive cells. The considerable noise in non-Abelian clusters may be attributed to the change in C_2 contribution from different Bloch states that are included at larger L . Nonetheless, the best-fit curves suggest that, for large L , $-C_2^{\text{cl}}/N$ converges to 1.0 and 1.35, respectively.

Since \mathcal{S} anticommutes with $\mathcal{P}^E\mathcal{T}$ (i.e., the “sublattice parity is odd” per the terminology of Ref. [51]), the Hamiltonian $H_k^{(2,1)}$ belongs to nodal class DIII at $m = 0$. The sublattice symmetry thereby reduces the codimension for node formation to $\mathfrak{d} = 2$ [51], which implies that the nodal manifold becomes four-dimensional in $\text{BZ}^{(2,1)}$ (so that it completely fills the three-dimensional projection in the $m = 0$ panel of Fig. S3), and the DOS scaling turns into $\rho(E) = \int d^2k_{\perp} \delta(E - v|k_{\perp}|) \propto E$ where we integrate over the two directions locally perpendicular to the nodal manifold. This theoretical prediction is consistent with the observed drop in the numerically extracted exponent visible in Fig. S4.

Appendix G: Flux insertion in PBC clusters

To explore the topological response of finite systems to external fields, we focus on small PBC clusters and compute the cluster-specific second Chern number C_2^{cl} by threading fluxes along the four translation directions. Namely, we append a phase to the inter-site transition matrices T_j in Eq. (A9) as $T_j \rightarrow T_j e^{i\phi_j}$ with $\phi = \{\phi_j\}_{j=1}^4 \in [0, 2\pi)^4$. We consider Abelian and non-Abelian clusters with $N = 16, 18, 20$ primitive cells. For the non-Abelian clusters, the non-Abelian states constitute $1/2, 2/3$, and $4/5$ of the total eigenstates, respectively.

In the flux space, the total second Chern number of a multiplet of n_f filled bands (which may have mutual degeneracies) is [45]

$$C_2 = \frac{1}{32\pi^2} \int_{\mathbb{T}^4} d^4\phi \epsilon^{ijklm} \text{Tr}(F_{jk}F_{lm}), \quad (\text{G1})$$

where

$$F_{jk} = \frac{\partial A_k}{\partial \phi_j} - \frac{\partial A_j}{\partial \phi_k} + i[A_j, A_k] \quad (\text{G2})$$

is the non-Abelian Berry curvature in the plane spanned by directions j and k , and

$$A_j^{\alpha\beta} = \langle \psi_{\alpha}(\phi) | \frac{\partial}{\partial \phi_j} | \psi_{\beta}(\phi) \rangle \quad (\text{G3})$$

is the non-Abelian Berry connection computed from eigenstates $|\psi_{\alpha}(\phi)\rangle$ with $\alpha = 1, \dots, n_f$. Here ϵ^{ijklm} is the Levi-Civita symbol in 4D with an implicit sum over repeated indices and the integration is over the 4-torus \mathbb{T}^4 defined by ϕ . We follow Ref. [49] for the numerical computation of C_2 .

The dependence of C_2^{cl} on the grid size L in Fig. S5 shows that while the Abelian clusters have $C_2^{\text{cl}}/N = C_2$ in agreement with the band theory, positioning of the Bloch states with respect to the nodal manifold influences C_2^{cl} in non-Abelian clusters.